Research Square

Preprints are preliminary reports that have not undergone peer review.
They should not be considered conclusive, used to inform clinical practice,
or referenced by the media as validated information.

A multidimensional “omics” approach reveals biased signaling through flg22- and UDP-glucose-induced, AtRGS1-driven signaling circuits

Justin Walley

jwalley@iastate.edu

Iowa State University https://orcid.org/0000-0001-7553-2237

Zhi Li

Iowa State University

Eduardo Simoni

Universidade Federal de Viçosa

Jing Yang

University of North Carolina at Chapel Hill

Christian Montes

Iowa State University https://orcid.org/0000-0003-1249-2308

Alan Jones

University of North Carolina at Chapel Hill https://orcid.org/0000-0002-2365-6462

Article

Keywords:

Posted Date: November 3rd, 2026

DOI: https://doi.org/10.21203/rs.3.rs-11281673/v1

License: This work is licensed under a Creative Commons Attribution 4.0 International License.
Read Full License

Additional Declarations: There is **NO** Competing Interest.

Abstract

Different cellular inputs into a central signaling core elicit different outputs in a process called biased signaling. Often this occurs by imprinting the signaling core with a phosphorylation bar code, functionally analogous to a microprocessor. The bacterial peptide flg22 and UDP-glucose both utilize a heterologous G protein core that contains a 7-transmembrane RGS protein, AtRGS1, to mediate changes differentially in plant defense and growth. Both flg22 and UDP-glucose launch rapid endocytosis of AtRGS1 at the plasma membrane but the destination and route are signal specific. flg22 directs plasma membrane AtRGS1 to the nucleus followed by different gene expression profiles. UDP-glucose does not direct AtRGS1 to the nucleus and does not elicit transcriptional reprogramming. Instead, UDP-glucose causes a massive, time-dependent restructuring of the G protein complex that likely traffics to the endosomal compartment. Associated with these two outcomes are phosphorylation bar codes that correlate with different patterns of AtRGS1-associated partners over time.

INTRODUCTION

The Regulator of G protein Signaling protein in Arabidopsis, AtRGS1, is a receptor-like, modulator of G-protein complex-regulated plant cell proliferation. Loss of AtRGS1 confers increased cell elongation in etiolated hypocotyls and increased cell production[1–5], positing that a growth-promoting sugar or a sugar metabolite plays an inhibitory role in AtRGS1 function[6]. For nearly two decades, the experimental evidence suggested that glucose is the signal molecule that directly regulates AtRGS1 de-repression of G-protein signaling by inducing removal of AtRGS1 from the G protein complex by endocytosis[7–10]. However, it is not likely that glucose is the AtRGS1 agonist because: **1)** several L-stereo-sugars, both, mono and disaccharides across a spectrum of structures cause AtRGS1-dependent activation of G signaling[9]. These molecules lack a common structure to explain a single orthosteric binding site. **2)** The high concentration of sugars (mM amount), while not hypertonic, that are needed for activation is inconsistent with specific binding to AtRGS1 above thermal noise. **3)** Mathematical modeling of G protein activation in Arabidopsis proposes that there is a “molecule X” immediately downstream of glucose that is the AtRGS1 ligand[11]. These observations point to a common sugar metabolite or catabolite that is produced from various sugars at a physiological concentration 1000-fold lower than the starting concentration of the sugar substrate. Recent studies from our group showed that the sugar signal molecule is UDP-glucose (UDPG), a metabolite of D-glucose, sucrose, and other sugars[12]. UDPG binds to AtRGS1 with a physiologically-relevant affinity (Kd = 17 μM) and induces AtRGS1 responses with an EC_{50} of 15 μM. Consistent with this, physiological levels of UDPG induce rapid AtRGS1 endocytosis.

The story is far more complicated because flg22, a bacterial elicitor of plant immune responses, also induces AtRGS1 endocytosis[13]. flg22 is a 22-amino acid peptide that shares no structure with UDPG. Rather, evidence is mounting that two ligands operate in a biased signaling pathway[14], both operating on AtRGS1, one indirectly by binding a receptor kinase[15] that phosphorylates AtRGS1[16] and the other binding AtRGS1 directly[12]. This is illustrated in Fig. 1A. Both flg22 and UDPG cause rapid AtRGS1

phosphorylation (**Supplemental Information Figure S1**)[12,17,18]. AtRGS1 endocytosis is driven by two separate pools of PM-localized AtRGS1: sugar-induced endocytosis requires both clathrin- and sterol-dependent processes while flg22 induced endocytosis of AtRGS1 is solely clathrin mediated[13]. Cellular changes downstream of AtRGS1 are also dependent on these input signals; flg22 and UDPG activate the MAPK cascade with different kinetics and requirements. Moreover, flg22, but not UDPG **(**Fig. 1H, **Supplemental information Figure S2)**, elicits a strong Reactive Oxygen Burst (ROS). These observations prompt the question of how can two or more signal inputs that propagate through the same signaling core elicit such different outputs? Does phosphorylation of the core encode information on this signaling bias?

AtRGS1 dynamically interacts with co-receptor kinases FLS2/BAK1 and BIR1/BAK1 in a phosphorylation-dependent manner to regulate immune and sugar signaling in Arabidopsis[19]. In its resting state, AtRGS1 is associated with BIR1, preventing its interaction with BAK1[19]. Upon flg22 perception, FLS2 dimerizes with BAK1, triggering phosphorylation events that lead to the displacement of BIR1 and the recruitment of AtRGS1 to BAK1[19]. This interaction is facilitated by the phosphorylation of AtRGS1 at Ser428 by BAK1, which acts as a switch for its conformational shift and subsequent G-protein activation[20]. Additional phosphorylation at Ser431 by BIK1/PBL1[18] and at Ser435/436 by WNK8/10[7] creates a phospho-barcode that integrates multiple signaling pathways and promotes AtRGS1 endocytosis. FRET analyses revealed a precise timeline where AtRGS1-BIR1 dissociation peaks at 3 minutes post-stimulation, followed by transient AtRGS1-BAK1 interaction, with AtRGS1 internalization occurring by 20 minutes [19]. All these discoveries imply an AtRGS1 phospho-barcode that enables the fine-tuned regulation of immune responses and sugar signaling, allowing plants to rapidly adapt to external stimuli through dynamic control of G-protein activation.

In this study, we employed root tissue for both physiological and technical reasons. Because our approach generates “omic” data that requires large amounts of tissue that must be harvested in less than 10 seconds, we developed a growth format to facilitate these constraints. Roots respond to flg22 and sugars. Externally applied flg22 affects plant root development[21–23]. The loss of UDPG metabolic related enzymes showed altered root development which implies that UDPG participates in plant root growth[24–27]. Sucrose synthase, an enzyme that produces UDPG, binds RGS1[12]. We showed that both UDPG and flg22 signals work through AtRGS1. This positioned us to investigate how different cellular inputs into a central signaling core elicit different outputs in a process called biased signaling[13,14].

Toward this, flg22 and UDPG were applied to roots and multi-omic profiles were generated including transcriptome, proteome, phosphoproteome, AtRGS1-proxitome, and AtRGS1-interactome. These datasets were then compared to time-dependent AtRGS1 phosphorylation and plasma membrane AtRGS1 cellular trafficking to the nucleus. The entire time course covered the seconds to minutes during which AtRGS1 moves from the plasma membrane to the nucleus and other cellular compartments in a signal-dependent manner. We observed that flg22 involves a massive AtRGS1-dependent reprogramming of the phosphoproteome whereas UDPG sets in motion a massive change in the composition of the

signaling complex. The identities of the phosphoproteins and the dynamic core components points to the mechanism underlying these profound cellular changes.

METHODS

Root growth assay

WT (Col-0) *Arabidopsis thaliana* and *rgs1*-2 mutant seeds were sterilized and then sown on solid 1/2X Murashige and Skoog (MS) medium with 0.7% agar and 0.5% sucrose and stratified at 5°C for 2 days, then grown under 16h light/8h dark at 22°C for 4 days. Seedlings with the same root length (~ 3cm) were then chosen and transferred to treatment plates for an additional 5-day growth. The treatment plates were solid 1/2X Murashige and Skoog (MS) medium with 0.7% agar but no sucrose, treatment plates contained either flg22 or UDPG as indicated in the result. After 5-day growth for the treatment, plates were scanned, and root lengths were measured with Fiji software. Statistics were performed using the Student's t-test followed by a Benjamini-Hochberg (BH) adjustment. More than twelve independent biological replicates were included for each combination of plant line and treatment.

Optimization of response time for elicitation.

All inductions for this study were performed at the same time of day, 8 h post "lights on" in the chamber. This is because we found that under our growth conditions in lab chambers, the responsiveness of flg22 to induce a ROS burst in Arabidopsis is highly dependent on the time of day. This is shown in **Supplemental Information Figure S3**. The response is lowest in the early morning and increases to a maximum level by early evening (**Supplemental Information Figure S3A**). A second elicitation does not exceed the first elicitation maximum obtained at the time of day when the first was given indicating memory in the system. The response is not likely circadian. When plants are grown in a day-night cycle and moved to constant darkness for one day prior to the test period, the previously observed increase over the day is no longer observed (**Supplemental Information Figure S3B**). This suggests that the response is related to the diel cycle and not the circadian clock. Therefore, we tested the responsiveness to flg22 over the day using the circadian clock mutants *cya1* and *lhy20*. Genetic ablation of the circadian clock did not disrupt the responsiveness dynamics (**Supplemental Information Figure S3C**). Therefore, based on these data, all experiments were started at 2 pm Eastern Time.

Plasma membrane (PM) localized AtRGS1 depletion assays

Transgenic plant seeds expressing 35S:FAPβ-AtRGS1-APEX2 were sterilized, and then sown in liquid 1/2X MS medium with 0.5% sucrose and stratified at 5°C for 2 d, then grown under 16h light/8h dark at 22°C for 13 d. On day 13, the MS medium was replaced with sterilized ddH_2O and then all seedlings were grown in the dark for 24 h. βGREEN-np membrane impermeant fluorogen (SKU: βGREEN-np-010, Spectragenetics) was prepared according to the manufacturer's instruction. Seedlings were first placed in sterilized ddH_2O with 100nM fluorogen for 15 min then a wash out was performed with sterilized

ddH_2O 3 times. After the wash out, seedlings were treated by sterilized ddH_2O containing either 100 nM flg22 or 123 μM UDPG for different times as indicated. Image acquisition was performed with a Zeiss LSM880 AxioObserver (Zeiss Microscopy, Oberkochen, Germany) confocal laser scanning microscope. The excitation wavelength was 514 nm with a 4% laser energy and the detection wavelength was 520–540 nm. A C-Apochromat 40x/1.2 water immersion objective was used for image collection. Image data was processed by ZEN blue 2.3 lite version, and statistics were done with the Student's t-test followed by a BH adjustment. Four independent biological replicates were included for each combination of treatment, and time point.

Optimization of APEX2-based proximity labeling efficiency

Col-0 and transgenic plant seeds expressing 35S:FAPβ-AtRGS1-APEX2 were sterilized and then sown in liquid ½ X MS medium with 0.5% sucrose and stratified at 5°C for 2 d, then grown under 16h light/8h dark at 22°C for 13 days. On day 13, the medium was replaced with ½ X MS medium without sucrose, and then all seedlings grown in darkness of 24 h. All the test treatments were done on day 14 as described in the results section. Total proteins were extracted with RIPA buffer (10 mM Tris/Cl pH 7.5, 150 mM NaCl, 0.5 mM EDTA, 0.1% SDS, 1% Triton™ X-100, 1% deoxycholate, 1X protease inhibitor cocktail (Roche cOmplete™ Protease Inhibitor Cocktail), protein concentration was measured by Bradford assay (Thermoscientific, Catalog number: 23246), and the same amounts of total proteins were then used for biotinylated protein enrichment. Biotinylated protein enrichment was performed according to Zhang et al.[28]. Enriched proteins were resuspended with 2X Laemmli loading buffer and heated to 95^{O}C for 5 min before being loaded on 10% in-house prepared SDS-PAGE gels for separation. Separated proteins were then transferred to nitrocellulose membrane (Millipore, Catalog number: 1620115) using the Mini-PROTEIN® Tetra System (Bio-Rad). Membranes were blocked for 1 h in 3% BSA in PBST and then incubated with the streptavidin-HRP (Abcam, Catalog number ab7403; 1:5000 dilution). Bands were visualized using SuperSignal™ West Pico PLUS Chemiluminescent Substrate (ThermoFisher, Catalog number 34577) according to the manufacturer's instruction. Chemiluminescent signals were acquired using a Lumazone imaging system (Roper Bioscience) equipped with a PIXIS 1024 CCD camera (Teledyne Princeton Instruments). Using this protocol, we optimized the time and concentrations of reagents used for proximity labeling as described in **Supplemental Information Figure S4**.

Transcriptomes - RNA-seq

For the transcriptome experiment, Col-0 and *rgs1-2* mutant seeds were sterilized and then sown and grown as described in the section labeled "Optimization of APEX2-based proximity labeling efficiency". On day 14, flg22 or UDPG treatment was performed as indicated in the results section and treated roots were then collected and frozen with liquid nitrogen within 10 sec. Total RNA from treated plant roots were extracted using Monarch® Total RNA Miniprep Kit (T2010S) following manufacturer recommendations and extracted RNA was used for preparing the cDNA library used in sequencing

facility. Sequencing was performed on an Illumina Nextseq 2000 system using P4 flow cells to generate 2×100 bp paired end reads at the High throughput sequencing facility from UNC at Chapel Hill. Four independent biological replicates were included for each combination of plant line, treatment, and time point.

Interactomes - AtRGS1-YFP Immunoprecipitation coupled with Mass Spectrometry (IP-MS, “pulldown”)

Transgenic plant seeds expressing 35S:AtRGS1-YFP were sterilized and then sown and grown as described in the section labeled “Optimization of APEX2-based proximity labeling efficiency”. On day 14, flg22 or UDPG treatment was performed as described in the Results section and treated roots were then collected and frozen in liquid nitrogen in less than 10 sec. Total proteins were extracted and the same amount of total protein was then used for pulldown. GFP-Trap magnetic agarose (ChromoTek) was used to immunoprecipitate GFP-fusion AtRGS1 from total proteins according to the protocol. Protein samples from pulldown were cleaned and processed into peptides with S-Trap™ micro-MS sample prep kit (Protifi) per the manufacturer’s instructions. Peptides were desalted using SepPack C18 columns (Waters™). Desalted peptides were then labeled with TMTpro mass tag labeling reagents and kits (Thermoscientific, Cat. # A52045)[29]. Labeled peptides were then pooled and desalted with SepPack C18 columns. After these steps, peptides were then fractionated with the Pierce high pH reversed-phase peptide fractionation kit (Thermoscientific, Cat. #: 84868) according to the kit instructions before loading to mass spectrometry. Three independent biological replicates were included for each combination of plant line, treatment, and time point.

Proxitomes - APEX2-based proximity labeling

Transgenic plant seeds expressing 35S:FAPβ-AtRGS1-APEX2 and Col-0 seeds were sterilized and then sown and grown as described in Supplemental Information S3. All treatments and root sample collections were done on day 14. All plants were incubated with 100 μM biotin-phenol for 30 min. For mock groups, for the following 30 s, 100 μM H_2O_2 was used to trigger background proximity labeling before roots were harvested and frozen in liquid nitrogen within 10 sec. For treatment groups, plants were treated with flg22 or UDPG before starting the proximity labeling reactions and sample harvest. Total proteins extraction was the same as the AtRGS1-YFP pulldown experiment. Biotinylated proteins enrichment plus the on-bead digestions were done according to Zhang et al[28]. Peptide sample preparation was performed according to the description for the AtRGS1-YFP pulldown experiment. Three independent biological replicates were included for each combination of plant line, treatment, and time point.

Phosphoproteomes

Col-0 and *rgs1-2* mutant seeds were sterilized and then sown and grown as described in the section labeled “Optimization of APEX2-based proximity labeling efficiency”. On day 14, flg22 or UDPG treatment was performed as described in the Results and treated roots were then collected and frozen in liquid nitrogen within 10 sec. Total protein isolation and phosphopeptide enrichment were done according to the published protocol [29]. Desalted peptides were divided into two groups, peptides from the first group were labeled with TMTpro mass tag labeling reagents and kits (Thermoscientific, Catalog number: A52045). Labeled peptides were then pooled and desalted with SepPack C18 columns, after these steps, phosphopeptides were enriched and then fractionated with Pierce high pH reversed-phase peptide fractionation kit (Thermoscientific, Catalog number: 84868) according to the kit instructions before loading to mass spectrometry for a data dependent acquisition (DDA) based phosphoproteome study. Peptides from the second group were subjected to phosphopeptide enrichment individually according to the MagReSyn® Zr-IMAC kit (ReSyn Biosciences, Catalog number: MR-ZRM005), obtained phosphopeptides then used for data independent acquisition (DIA) based phosphoproteome study. For the DDA-based phosphoproteome experiments, six independent biological replicates were included for each combination of plant line, treatment, and time point; for the DIA -based phosphoproteome experiments, three independent biological replicates were included for each combination of plant line, treatment, and time point except for 10 min flg22 treated WT plants which only had two independent biological replicates.

Global Proximity Labeling and IP LC-MS/MS

Chromatography was performed on a Thermo Vanquish Neo UHPLC in “heated trap-and-elute, backward flush” mode. Peptides were desalted and concentrated on a PepMap Neo trap column (300 µM i.d. x 5 mm, 5 µm C18, 100 Å µ-Precolumn, Thermo Scientific) at a flow rate of 10 µL min-1. Sample separation was performed on a 110 cm Micro-Pillar Array Column (µ-PAC Neo, Thermo Scientific) with a flow rate of ~ 300 nL min-1 over a 125 min reverse phase active gradient (80% ACN in 0.1% FA from 7.2% to 24% over 90 min, from 24% to 44% for 35 min). Followed by a column/trap wash at 80% ACN for 10 min. Eluted peptides were analyzed using a Thermo Scientific Orbitrap Exploris 480 mass spectrometer with a FAIMS pro Duo interface installed, which was directly coupled to the UHPLC through an Easy Spray Ion source (Thermo Scientific). Data dependent acquisition was obtained using Xcalibur 4.0 software in positive ion mode with a spray voltage of 2.1 kV, a capillary temperature of 280°C, an RF of 45, FAIMS compensation voltages (CVs) of -55, and − 75, and a total carrier gas flow of 4.2 l/min. MS1 spectra were measured at a resolution of 120,000, an automatic gain control (AGC) of 3e6 with maximum ion time set on “Auto”, and a mass range of 400–1500 m/z. A cycle time of 0.8s was used on each CV to capture triggered MS2 at a resolution of 15,000 with the “Turbo TMTpro” setting on. A fixed first mass of 110 m/z. An AGC of 2e5 with a maximum ion time of 22 ms, a normalized collision energy of 32, and an isolation window of 0.7 m/z were used. Charge inclusion was set to 2–6. MS1 that triggered MS2 scans were dynamically excluded for 30 sec.

DDA-based phosphoproteome

Chromatography was performed on a Thermo Vanquish Neo UHPLC in “heated trap-and-elute, backward flush” mode. Peptides were desalted and concentrated on a PepMap Neo trap column (300 µM i.d. x 5 mm, 5 µm C18, 100 Å µ-Precolumn, Thermo Scientific) at a flow rate of 10 µL min-1. Sample separation was performed on a 110 cm Micro-Pillar Array Column (µ-PAC Neo, Thermo Scientific) with a flow rate of ~ 300 nL min-1 over a 125 min reverse phase active gradient (80% ACN in 0.1% FA from 8% to 28% over 90 min, from 28% to 50% for 35 min). Followed by a column/trap wash at 80% ACN for 10 min. Eluted peptides were analyzed using a Thermo Scientific Orbitrap Exploris 480 mass spectrometer with a FAIMS pro Duo interface installed, which was directly coupled to the UHPLC through an Easy Spray Ion source (Thermo Scientific).

This data-dependent acquisition was obtained using Xcalibur 4.0 software in positive ion mode with a spray voltage of 2.2 kV, a capillary temperature of 280°C, an RF of 45, FAIMS compensation voltages (CVs) of -45, and − 60, and a total carrier gas flow of 4.2 l/min. MS1 spectra were measured at a resolution of 120,000, an automatic gain control (AGC) of 3e6 with maximum ion time set on “Auto”, and a mass range of 350–1400 m/z. The top 15 scans for each CV were used to capture triggered MS2 at a resolution of 45,000 with the “Turbo TMT” setting off. A fixed first mass of 100 m/z. An AGC of 3e6 with a maximum ion time of 96 ms, a normalized collision energy of 33, and an isolation window of 0.7 m/z were used. Charge inclusion was set to 2–6. MS1 that triggered MS2 scans were dynamically excluded for 20 s.

DIA-based phosphoproteome

Chromatography was performed on a Thermo Vanquish Neo UHPLC in “heated trap-and-elute, backward flush” mode. Peptides were desalted and concentrated on a PepMap Neo trap column (300 µM i.d. x 5 mm, 5 µm C18, 100 Å µ-Precolumn, Thermo Scientific) at a flow rate of 5 µL min-1. Sample separation was performed on a 25 cm Aurora Ultimate Column (Ionopticks) with a flow rate of ~ 300 nL min-1 over a 120 min reverse phase active gradient (80% ACN in 0.1% FA, from 5% to 28% over 109 min and from 28% to 62.5% in 11 min). Followed by a column/trap wash at 78% ACN for 10 min. Eluted peptides were analyzed using a Thermo Scientific Orbitrap Exploris 480 mass spectrometer, which was directly coupled to the UHPLC through an Easy Spray Ion source (Thermo Scientific). Data independent acquisition was obtained using Xcalibur 4.0 software in positive ion mode with a spray voltage of 1.7 kV, a capillary temperature of 280°C, and an RF of 45. MS1 spectra were measured at a resolution of 60,000, an automatic gain control (AGC) of 2.25e6 with maximum injection time set on “Auto”, and a mass range of 400–900 m/z. Forty nine DIA acquisition windows of 13.7m/z with 1Da overlap were measured at a resolution of 15,000, an automatic gain control (AGC) of 8e6 with auto maximum ion time, over a precursor mass range of 375–1043 m/z. A scan range 145–1450 m/z and normalized collision energy of 29 were used.

Omics data analysis

For the transcriptome data analysis, FastQC was used for raw data quality control, and low-quality reads and adapters were removed using Trimmomatic[30]. The cleaned reads were aligned to the reference

genome Araport11 of *Arabidopsis thaliana* using HISAT2, and feature counts[31] was used to obtain transcript levels. Differential expression analysis and likelihood ratio tests were carried out using DESeq2[32] to identify significantly differentially expressed transcripts and AtRGS1-dependent transcripts. Gene ontology and pathway enrichment analyses were performed using ClusterProfiler[33]. The Wald test with Benjamin-Hochberg (BH) adjustment integrated in DESeq2[32] was chosen as the statistical approach.

Raw data of the AtRGS1-YFP pull down samples subjected to LC-MS/MS was first analyzed with Maxquant[34] version 2.5.2.0. Spectra were searched against the Arabidopsis TAIR10 proteome, which was complemented with reverse decoy sequences and common contaminants by MaxQuant. The "Match between runs" function was set to false, FAIMS-Reporter-MS2 was chosen as the run type, Trypsin/P and LysC were chosen as the digestion enzyme. The proteinGroups.txt files generated by Maxquant were used for further analysis. Protein quantities from each channel were first normalized according to the AtRGS1 intensity within the same channel then imported into DEqMS[35] for differential expression analysis. Moderated Student t-test with BH adjustment integrated in the DEqMS[35] was used as the statistical approach.

For the DDA generated phosphoproteome data, raw data from LC-MS was first analyzed with Maxquant[34] version 2.5.2.0. Spectra were searched against the Arabidopsis TAIR10 proteome, which was complemented with reverse decoy sequences and common contaminants by MaxQuant. Match between runs function was set to false, FAIMS-Reporter-MS2 was chosen as the run type, Trypsin/P and LysC were chosen as the digestion enzyme, Phospho (STY) was added to the variableModification. The Phospho (STY)Sites.txt file generated by Maxquant was imported into Perseus[36] where contaminant and reverse decoy hits were removed and phosphosite quantities were normalized with the internal reference scaling method[37]. Normalized data were then imported into DEqMS[35] for differential expression analysis. Student t-test with BH adjustment integrated in the DEqMS[35] was used as the statistical approach.

For the DIA generated phosphoproteome data, raw data from LC-MS was first analyzed with Spectronaut® version 20.1.250624.92449 (BIOGNSYS). The directDIA was chosen as the analysis type, BGS Phospho PTM Workflow was used. Spectra were searched against the Arabidopsis TAIR10 proteome, Trypsin/P and LysC were chosen as the digestion enzyme, Carbamidomethyl (C) was added to Fixed Modifications, Acetyl (Protein N-term), Oxidation (M), Phospho (STY) were added to the variable Modifications.

Network establishment and multi-omics integration

AtRGS1-dependent phosphopeptides were identified using two complementary filtering criteria. Filter A selected phosphopeptides that exhibited a significant response (adjusted $P < 0.05$) in WT plants but not in *rgs1*-2 plants (adjusted $P > 0.05$) under the same treatment condition, or that were significantly regulated in both genotypes but displayed opposite or divergent response trends. Filter B selected

phosphopeptides that exhibited a significant response (adjusted P < 0.05) in *rgs1*-2 plants but not in WT plants (adjusted P > 0.05), or that were significantly regulated in both genotypes but showed opposite or divergent response trends. Phosphopeptides that passed either Filter A or Filter B were subjected to Pearson correlation analysis separately in WT and *rgs1*-2 datasets. Protein pairs with a Pearson correlation coefficient (r) greater than 0.653 were classified as highly correlated. Highly correlated protein pairs involving kinases or phosphatases identified in WT and *rgs1*-2 plants were combined and used to construct the AtRGS1-dependent phosphorylation network **(Supplemental Information Figure S5A)**.

For the multiomics data integration of phosphoproteome and transcriptome data, we used Spatiotemporal Clustering and Inference of Omics Networks (SC-ION)[38,39]. AtRGS1-dependent phosphosites derived from proteins involved in translational regulation were selected as candidate regulators, while AtRGS1-dependent differentially expressed genes identified from the transcriptomic dataset were selected as targets. The regulator and target datasets were integrated into SC-ION to infer regulatory relationships and evaluate their correlation strength. Regulatory interactions exhibiting strong correlation were retained and combined to construct an AtRGS1-dependent regulatory network **(Supplemental Information Figure S5B)**. All the SC-ION settings were kept as default.

RESULTS

Signaling bias in cell behavior: AtRGS1 is involved in Arabidopsis root responses to external UDPG and flg22.

For reasons discussed above, we developed a new hydroponic format to enable rapid harvest and flash freezing of root tissue. While it is well established that flg22 and sugars, including UDPG, cause AtRGS1-dependent changes in starved seedlings, less is known if roots behave the same, especially under the new growth format used in this study. Therefore, we tested whether UDPG and flg22 responses are observed under these new conditions. The concentrations chosen for this study are based on studies of EC50s[12,40]. Ten times the EC50 is typically the lowest concentration that induces a full response. In a dose-dependent manner, both UDPG (equal or higher than 123 μM) and flg22 (equal or higher that 50 nM) inhibited root growth in a genotype-dependent manner. *rgs1-2* roots were longer compared to WT roots under UDPG treatment while shorter than WT roots under the flg22 treatment **(Supplemental Information Figure S6A and S6B)**. Moreover, AtRGS1 acts as a positive modulator of UDPG inhibition of root growth and oppositely as a negative modulator of flg22 inhibition of root growth. This indicates that AtRGS1 functions in root elongation in response to external UDPG and flg22, and that the molecular mechanisms behind AtRGS1 mediated root development responses are biased. At least part of the mechanism lies in different patterns of transcriptional responses to the two signals and likely that other changes in cell behavior occur to bring about this signaling bias.

To address this question, we ask if both flg22 and UDPG affect AtRGS1 localization in the root? We used a fluorogen-activating protein beta[41,42] (FAPβ) tagged AtRGS1 (FAPβ-AtRGS1) expression line to monitor changes in the plasma membrane pool of AtRGS1. This novel method was developed for AtRGS1 to increase the sensitivity and the quantitation of FAPβ-AtRGS1 endocytosis by eliminating the cytoplasmic background signal. Moreover, with this method, only the PM-pool of FAPβ-AtRGS1 is labeled with the cell-impermeant fluorophore, thus we can conclude that internal fluorescent FAPβ-AtRGS1 originated from the plasma membrane. Both flg22 and UDPG caused FAPβ-AtRGS1 endocytosis with UDPG generating a greater extent than flg22 as has been thoroughly quantitated for the hypocotyl and cotyledon with flg22 and monosaccharides[11,13]. Internalization of FAPβ-AtRGS1 by UDPG is sustained over the time course, whereas by flg22, nuclear FAPβ-AtRGS1 is transient (Fig. 1B).

FAPβ-tagged AtRGS1 translocated from the plasma membrane to nuclei (Fig. 1C and 1D). FAPβ-AtRGS1 was evenly distributed in the nucleoplasm (Fig. 1D), although FAPβ-AtRGS1 still appeared to be associated with interphase chromatin (Fig. 1E). Quantitation of this nuclear localization was determined by identifying nuclei under differential interference contrast microscopy that were either fluorescent or not (Fig. 1D). In the absence of added signal (flg22 or UDPG), there is a baseline amount of FAPβ-AtRGS1 in the nucleus (Fig. 1F). flg22, but not UDPG, increased translocation of FAPβ-AtRGS1 from the plasma membrane to the nucleus compared to the control (Fig. 1F). At this point, the trafficking route of plasma membrane FAPβ-AtRGS1 initiated by UDPG (Fig. 1B) is not clear. This is addressed later.

Differences in AtRGS1 localization to the nucleus by flg22 vs. UDPG are not likely due to differences in dynamics. This is shown by examining the time dependency of action (Fig. 1G). flg22 and UDPG showed strongly biased signaling regarding ROS production, a signature response in plant immunity. flg22 induced a robust ROS transient in WT (Fig. 1H). The negative control, *fls2*, indicated no flg22-induced ROS production, and the *rgs1*-2 mutant produced more ROS than WT, as has been shown previously (**Supplemental Information Figure S2A**). In contrast, UDPG did not induce ROS in WT, but a small response was detectable in the *rgs*1-2 null mutant (**Supplemental Information Figure S2B**).

Signaling bias in transcriptional programming: AtRGS1-dependent flg22 and UDPG regulation of steady-state levels of transcripts.

It is well documented that specific external stimuli trigger the translocation of RGS proteins, and receptors residing on the PM, into the nucleus[43–46], thereby regulating cellular transcriptional responses[47,48]. As shown above (Fig. 1F), flg22, but not UDPG, increases the pool of AtRGS1 in nuclei above the basal state. We determined if these signal-dependent differences in nuclear translocation are reflected in transcriptional profiles (**Data Set S1 Transcriptome, sheet LFC of WT and rgs1-2**). Time sequence analysis for the transcriptomes of WT and *rgs1-2* mutants under flg22 or UDPG treatment was performed using RNA-seq. Three-dimensional principal component analysis using normalized-count data showed that flg22 treatment led to more widespread transcriptional changes than UDPG treatment in both WT and *rgs1-2* (Fig. 1I). The first three principal components accounted for 61.4% of the total variance (PC1: 30.9%, PC2: 16.9%, PC3: 13.6%), suggesting that major biological differences across

conditions are well represented in the reduced dimensional space. flg22 treatment led to more widespread transcriptional changes than UDPG treatment in both WT and *rgs1-2* plants, and UDPG treatment had less of an impact on the differential response of WT and *rgs1*-2 plants compared to flg22 treatment. There were 1,355 differentially-expressed genes (DEGs) between 100 nM flg22-treated and untreated WT roots at 1 h with log2-fold changes greater than 1 (up-regulated) or less than − 1 (down-regulated) and adjusted p-values less than 0.05. The number of DEGs (3019) increased at 3 h in 100 nM flg22-treated roots compared to untreated WT roots. There were 239 DEGs in WT in the comparison of 123 µM UDPG-treated vs. untreated seedlings at 1h The number of DEGs (73) was less in the comparison of 3 h 100 µM UDPG-treated vs. untreated WT plants. All other comparisons showed that the transcriptional response to flg22 and UDPG differed dramatically in both extent and type of DEG. The increase in transcription induced by flg22 aligns with the flg22-increase in nuclear-localized AtRGS1.

flg22 causes transcriptional reprogramming in hydroponic roots (Fig. 2) and in seedlings[13,49–52]. Therefore, gene ontology (GO) processes that were over-represented among the UDPG and flg22-induced DEGs were identified by enrichment analysis. Consistent with the finding in Fig. 2, fewer enriched Biological Processes under UDPG treatment occurred than by flg22 treatment and there are more enriched Biological Processes at 3 h flg22 than at 1 h flg22 treatment. “Response to endoplasmic reticulum stress” was enriched under 3 h treatment with both flg22 or UDPG in both WT and *rgs1-2* plants. However, some biological responses were treatment- and/or AtRGS1-specific. For instance, some shared enriched biological processes under 1 h and 3 h flg22 treatment occurred in both WT and *rgs1-2* plants, including “immune response”, “response to hypoxia”, and “protein phosphorylation”.

Based on GO, both WT and *rgs1-2* showed strong immune responses to flg22, sharing most key defense pathways but with some genotype-specific nuances in timing and additional processes. The differences between WT and *rgs1-2* showed two strategies for plant immunity, where AtRGS1 prompts early responses to pathogens, because WT plants quickly activate salicylic acid (SA) defenses by reinforcing its cell wall, adjusting chromatin accessibility, and stabilizing specific transcription factors[53]. Under UDPG, both genotype’s responses were less synchronized initially but converged on common stress pathways, indicating that UDPG elicited a context-dependent response. Specifically, immune-related pathways (SA, Jasmonic acid signaling, programmed cell death, kinase signaling) were central in flg22-triggered DEGs, highlighting the activation of plant innate immunity. Energy-related and metabolic pathways such as hypoxia response, autophagy, and secondary-metabolite biosynthesis indicate that both treatments caused significant reconfiguration of the plant’s metabolism – namely, flg22 pushes the plant to invest energy into defense production and stress tolerance, and UDPG triggers management of internal stress and resource recycling. Time-course changes revealed that both treatments had an early phase focusing on signaling and preparation, followed by a later phase of execution and adjustment. The later phase of flg22 action encompassed a broad defensive program, whereas the later phase of UDPG action brought a stress-mitigation response. These insights together paint a picture of how two different stimuli overlap in activating the plant’s immune system but also engage distinct pathways reflective of their commission. Specifically, the enriched pathways identified here point to the critical biological

processes that the plant leverages for immunity (hormone signaling, cell death, antioxidant activity) and for coping with stress while fueling the defense response (autophagy, metabolic shifts). This illustrates the complex coordination between immune signaling and metabolic reprogramming in plant defense.

To obtain a quantitative difference in transcriptional reprograming between these two signals, we used the likelihood ratio test[54]. The likelihood ratio test is advantageous in RNA-seq analysis because it detects overall transcriptome changes across complex experimental designs, such as time courses or multi-factor studies, by comparing full and reduced models. After comparing the AtRGS1-dependent reduced models to the full model, we identified key components significantly influenced by AtRGS1. Specifically, 91 genes are AtRGS1 dependent in response to flg22 whereas only one gene, ATP-binding cassette B16 (ABCB16, AtG28360), was AtRGS1 dependent for UDPG treatment. The dynamics for these transcriptional changes fell in 8 bins as represented by typical genes for each trend (**Supplemental Information Figure S6C**). As seen in the heatmap with clustering in **Supplemental Information Figure S6D**, genes from cluster 1 were reduced under 1-h flg22 treatment in WT, but in *rgs1-2* they were upregulated. In cluster 2, genes increased more in WT than in *rgs1-2* after 3-h flg22 treatment. Genes in cluster 4 increased after 1-h flg22 treatment in WT but decreased in *rgs1-2*. These results suggest that AtRGS1 may play different roles in regulating gene expression, including activating, inactivating, and positive and negative feedback in regulation of gene expression.

Signal bias in the phosophoproteome: flg22-induced phosphorylation is dramatically regulated by AtRGS1.

Protein phosphorylation is known to play an important role in plant responses to external stimuli. AtRGS1 is phosphorylated in response to flg22 and UDPG treatment [18]. The phosphoproteome response to flg22 is better understood [13,49–52]. Thus, we performed phosphoproteome profiling to explore differences between flg22 and UDPG treatments and the assessed AtRGS1 involvement.

The flg22-induced phosphoproteome became apparent in WT (Col-0) plants within 5 minutes and increased at 10 minutes (Fig. 3A). In contrast, we did not detect a UDPG-triggered change in the phosphoproteome at either time point. The results from *rgs1*-2 mutants (Fig. 3B) had fewer decreased phosphosites compared to those of WT plants, indicating that AtRGS1 plays a role in the phosphoproteomic changes triggered by flg22. It should be noted that loss of the other core components of the AtRGS1/G protein complex also radically reduced the flg22-induced phosphoproteome[17]. An important question is whether the phosphoproteome differences between the two genotypes arise from phosphorylation of distinct proteins or from differential phosphorylation sites of the same proteins. Therefore, a heatmap of the changes was subjected to cluster analysis and shown in Fig. 3C. In cluster 1, some phosphosites that are upregulated in WT by flg22 decreased in *rgs1-2*, or verse vice in cluster 2 and 3. This shows that the vast majority of phosphosites clustered in the fold-change heatmap had opposite expression between the *rgs1*-2 mutant and WT roots. This clear opposite behavior indicates that AtRGS1 is acting as a positive regulator for these phosphosites. Most of the changes require AtRGS1 which is consistent with a previous published flg22-induced phosphoproteome

comparison between WT and a mutant lacking a functional G protein complex showing that the G protein complex is essential for flg22-induced phosphorylation[17].

Because AtRGS1 functions as a negative regulator of the heterotrimeric G protein complex[55], phosphoproteins regulated by G protein signaling may be influenced by both AtRGS1 and the G protein complex, potentially in opposing directions. To test this possibility, we compared our flg22-induced phosphoproteomic dataset with a previously published flg22 phosphoproteomic dataset generated from WT and a G protein complex knockout (*gpa1-4*, *agb1*-2, *agg1-1*, and *agg2-1* quadruple mutant designated hereafter as *quad*) plants[17] in order to identify phosphosites showing opposite responses between the two mutant backgrounds.

Significantly-regulated phosphosites (BH-adjusted $P < 0.05$) were identified independently in each dataset, and the intersection of these phosphosite sets was used to identify shared phosphorylation events. As a result, a total of 98 phosphosites were shared between the two phosphoproteomic datasets. Notably, most of these phosphosites displayed opposite response patterns in *rgs1*-2 and *quad* mutants (Fig. 3D). Among them were phosphosites derived from six transcriptional regulators and ten protein kinases. One notable example was MPK6, in which phosphorylation at Y223 increased after flg22 treatment in WT plants and was further elevated in *rgs1-2* plants, whereas this site did not respond to flg22 treatment in *quad* plants. MPK6 is a well-established regulator of plant immune responses[56], and T221/Y223 are located within its activation loop, where phosphorylation enhances kinase activity[56,57]. Together, these results suggest that loss of AtRGS1 and loss of the heterotrimeric G protein complex may differentially, and in some cases oppositely, regulate immune signaling outputs.

Motif enrichment analysis for phosphopeptides showed significant changes in WT plants and *rgs1*-2 mutants (**Data Set S2- Phosphoproteome, sheet LFC of WT and rgs1-2**). Before the motif enrichment analysis, phosphopeptides were binned into “increased” and “decreased” phosphorylation groups based on whether they were upregulated by the treatment or downregulated by the treatment. According to previous research on a meta-analysis for phosphoproteomics data[58], we then classified result kinase motifs into different types including SP, TP, and xSx (**Supplemental Information Table S1**). Motif SP is known as the target for kinases MPK, SnRK2, RLK, AGC, CDK, CDPK, SLK[58]. Only motifs SxS and SxxD from type xSx existed in the decreased phosphorylation group under 10 min flg22 treatment in WT plants (**Data Set S2- Phosphoproteome sheet LFC of WT and rgs1-2**), and SxS is the target of MPK, RLK, RLCK,CDK while SxxD is the target of SnRK1, AGC, and CDPK[58]. For the increased phosphorylation groups, WT and *rgs1*-2 showed shared motifs under each treatment. Motif SP was found in WT and *rgs1*-2 under 5 min of flg22 treatment, whereas under 10 min flg22 treatment Motif SP and TP were enriched in both lines. More interestingly, WT and *rgs1*-2 showed unique enriched motifs as well. Under 5 min flg22 treatment, a motif TP was enriched in WT but not in *rgs1*-2. Motif SxxxxSP was enriched in WT plants, motif SPR and SPxS were only enriched in *rgs1*-2 under 10 min flg22 treatment.

Given that phosphorylation regulates protein activity and interactions, we built an AtRGS1-dependent phosphorylation network using Pearson correlation with AtRGS1-dependent phosphopeptides. The

network has a high-confidence correlation threshold of R ≥ 0.653, based on the observed correlation between MPK6 (AT2G43790) and BSL3 (AT2G27210), which share an R-value of 0.653. This threshold is biologically justified, as a previous study demonstrated that BSL members (BSL2, BSL3, and BSU1) directly deactivate MPK6, effectively counteracting the linear MAPK signaling pathway[59]. Using this threshold, we isolated all protein kinases and phosphatases from the network along with their highly-correlated interacting proteins. The phosphorylation network contained an AtRGS1-dependent kinase/phosphatase network as shown in Fig. 3E. Proteins were classified into functional modules based on their annotated functions. Each module is labeled with the total number of nodes assigned to that module. The neighborhood connectivity value higher than 1 was only applied for the kinase and phosphatase modules. The protein indicated in each module is the node with the highest edge count with a value as indicated (# of grey lines). Within the kinase and phosphatase modules, we found several key kinases and phosphatases as central regulators of signaling pathways, each showing autophosphorylation (grey loops). Among the kinases, RAF15 (AT3G58640), PBS1 (AT5G13160), AT3G15220, AAK1 (AT2G32850), MAPK11 (AT1G01560), and PHOT1/NPH1 (AT3G45780) exhibit high betweenness-centrality and edge count, indicating their role as major hubs coordinating phosphorylation events. These kinases likely participate in MAPK signaling, lipid metabolism, and receptor kinase-mediated pathways, crucial for integrating nutrient and immune responses. Additionally, the phosphatase such as CPL1/RCF2/FRY2 (AT4G21670) display high betweenness-centrality, suggesting its importance in fine-tuning signal transduction. As discussed below, the resulting network showed the regulatory landscape of phosphorylation events influenced by AtRGS1 signaling, providing insights into how kinases and phosphatases modulate nutrient sensing, stress adaptation, and immune responses.

The resulting network connected the central kinase/phosphatase core to 15 modules each indicated with its hub protein. This hub is indicated by a magenta box and the total number of nodes (noted as proteins) in the module are indicated with a purple number (Fig. 3E). Aside from the module labeled “miscellaneous” (Fig. 3E, Misc module), the largest module was “gene regulation” with 71 nodes and a related module “zinc finger protein module” that contained 13 nodes. “Cellular trafficking” module was the next largest with 28 nodes. The carbohydrate module contained 23 nodes and the immune module had 9 nodes implying a fulcrum for the defense-growth tradeoff[60].

In addition to the proteins shown in Fig. 3E, the network also contains several protein kinases and phosphatases known to function in autophagy and brassinosteroid (BR) signaling pathways. Within the kinase module, we identified ATG1a, a key regulator of autophagy initiation[61]; BAK1, a core component of BR and defense signaling[62]; and MPK6, which is well known for its role in immune responses[56,57]. Within the phosphatase module, we identified two homologues of BSU1, BSL1 and BSL3, both of which are also involved in BR signaling (**Supplemental Information Figure S7**)[63,64]. Together, these observations suggest that AtRGS1-dependent phosphorylation networks may contribute to the integration of signaling pathways that coordinate plant growth and defense responses.

Signal bias in the AtRGS1 interactome: UDPG induces major shifts in conformational space; flg22 shifts dramatically less.

As shown in Fig. 1A, flg22 and UDPG launched the movement of AtRGS1 from the plasma membrane to different cellular compartments. This may mean that AtRGS1 sheds protein partners and associates with new ones as it traffics or that AtRGS1 moves as an intact complex. These alternatives may be signal dependent. To distinguish between these possibilities, we employed two omics approaches, APEX2-based proxitome and Immunoprecipitation coupled with Mass Spectrometry (IP-MS) base interactome, to profile dynamic complex membership.

Proximity labeling identifies proteins located closely to the cytoplasmic tail of AtRGS1, providing a snapshot of the local cytoplasmic AtRGS1 neighborhood. Consequently, changes in the proxitome reflect remodeling of proteins surrounding AtRGS1. In contrast, the interactome identified by IP-MS reflects proteins that remain associated with AtRGS1-containing complexes following biochemical isolation. Both approaches can detect direct and indirect interaction partners; however, proximity labeling captures proteins based on time-dependent, spatial proximity in living cells, whereas IP-MS identifies proteins that remain associated within AtRGS1-containing complexes under the pulldown conditions. Specifically, because biotin labeling occurs prior to cell lysis, proximity labeling is well suited to capturing transient or weak associations that may dissociate during protein extraction and therefore are underrepresented or absent in IP-MS analyses. Thus, these two approaches are complimentary[65–68]. The flg22- and UDPG-induced proxitome for both WT and At*RGS1APEX2 line* are provided in **Data Set S3 Proxitome, sheet AtRGS1APEX2 and sheet WT** and the IP-MS interactome is provided in **Data set S4 Interactome, sheet AtRGS1YFP**.

Both proxitome and interactome showed that UDPG induced a massive shedding from and re-orientation of proteins toward AtRGS1 (Fig. 4A and 4B). In contrast, flg22 caused relatively less change in the composition of the AtRGS1-G protein complex. To evaluate whether the proximity-labeling dataset contained a greater proportion of biologically meaningful signals than the WT control, we compared the p-value distributions of APEX2 and WT samples using empirical cumulative distribution function (ECDF) plots and a two-sample Kolmogorov–Smirnov (KS) test (**Supplemental Information Figure S4E**). The APEX2 dataset exhibited a significant leftward shift in its p-value distribution relative to WT ($D^+ = 0.1711$, $D^- = 0.0554$, $P < 2.2 \times 10^{-16}$), indicating an enrichment of low p-values in APEX2 (**Supplemental Information Figure S4E**). To determine an adaptive significance threshold, we calculated the 5th percentile of the P-value distribution from WT controls, defining the empirical cutoff as the value below which only 5% of WT P-values fall. This data-driven approach reduces background signal while accounting for the inherent biological variability of proximity-labeling data, rather than imposing a fixed statistical threshold. The resulting cutoff (P = 0.16) is indicated on the overlaid histogram of P-value distributions from AtRGS1-APEX2 and WT samples (Fig. 4C). Justification for this cutoff is elaborated in the Discussion. A higher density of proteins fell below this cutoff in the APEX2 samples than in WT, consistent with enrichment of treatment-responsive signals over background variation (Fig. 4C). Supporting the biological relevance of proteins identified near this 0.16 threshold, REM1.3 showed

decreased proximity to AtRGS1 following 10 min of UDPG treatment. Previous work using single-molecule kymograph analysis combined with variable-angle total internal reflection fluorescence (TIRF) microscopy showed stimulus-dependent colocalization between AtRGS1 and REM1.3 at the plasma membrane[69], indicating that their spatial association is dynamically regulated in response to signaling stimuli. Gene Ontology analysis of the APEX2 proxitome proteins revealed distinct functional enrichments across flg22 and UDPG treatments. Following flg22 treatment, proteins identified at both 5 and 10 min were strongly enriched for translation- and RNA-related categories, including translation, structural constituent of ribosome, cytosolic ribosome, RNA binding, mRNA binding, and nucleolus, suggesting rapid remodeling of the translational machinery in response to flg22. Additional enrichments at 10 min included cellular response to oxidative stress, ubiquitin binding, and vacuole, indicating a broader stress-associated and protein turnover response at the later time point (Fig. 4F and 4G). In contrast, UDPG treatment produced a more limited and distinct functional profile.

At 5 min, the enriched terms were restricted to kinase activity and ubiquitin protein ligase activity, whereas at 10 min, UDPG-associated proteins were enriched for terms related to organelle function and transport, including mitochondrion, plastid, chloroplast stroma, chloroplast envelope, transmembrane transport, and ATPase-coupled transmembrane transporter activity. Additional UDPG-enriched terms at 10 min included proteasome complex, ubiquitin-dependent protein catabolic process, protein folding, and structural constituent of ribosome (Fig. 4H). Together, these results suggest that flg22 predominantly triggers rapid changes in translation- and RNA-associated processes, whereas UDPG elicits a more limited response enriched in transport, organelle-associated, and protein homeostasis functions.

Keeping in mind that the AtRGS1 proxitome and the AtRGS1 interactome describe two different sets of proteins identified in proximity labeling and IP-MS experiments, respectively, the proximity labeling approach consistently detected more proteins across all treatments except for the decreased enrichment proteins after the 5 min UDPG treatment. IP-MS failed to detect any proteins for this treatment and no increased enrichment proteins after 10 min were found by the flg22 treatment (**Supplemental Information Table S2**).

When considered together with the transcriptome, phosphoproteome, proxitome and interactome datasets, these results indicate that flg22 and UDPG elicit distinct AtRGS1-associated molecular responses, reflected in differences in both the composition and temporal dynamics of proteins associated with AtRGS1. Specifically, flg22 induced more extensive changes in the transcriptome and phosphoproteome, whereas UDPG produced more pronounced changes in the AtRGS1 proxitome and interactome. Together, these findings support a model in which AtRGS1 participates in ligand-biased signaling responses to flg22 and UDPG.

To identify potential AtRGS1-interacted proteins involved in AtRGS1-mediated, biased-signaling pathways, we defined candidates as those that (1) showed a positive $\log_2$ fold change and a p-value < 0.16 in AtRGS1-APEX2 plants compared to WT plants under control conditions, and (2) had a p-value <

0.16 when comparing treatment vs. control in AtRGS1-APEX2 plants. (**Data Set S5 AtRGS1 Potential Partners**). Among these candidates there are: **1)** two G-proteins core components, GPA1 and AGB1; **2)** BAK1 and BRI1 involved in the BR signaling pathway; **3)** ATG8E involved in the autophagy pathway; and **4)** CDC5, MOS4, PRL1 which are known to form a complex involved in immune responses[70]. As shown in Fig. 4I, almost all proteins except ATG8E were significantly reduced after 10 min UDPG treatment, indicating a disassociation between AtRGS1 and these proteins. This also suggested that ATG8E may traffic together with AtRGS1. Only PRL1 showed a significant decrease under 10 min flg22 treatment, suggesting flg22 triggered disassociation between PRL1 and other proteins.

AtRGS1 phospho-bar code in signaling bias

Previous studies showed that phosphorylation of AtRGS1 is important for its function. For example, flg22 induced phosphorylation of AtRGS1 at Ser428 and Ser431 regulates immune responses by modulating the interaction between AtRGS1 and GPA1[18]. Another study using molecular dynamics simulations and *in vivo* assays demonstrated that phosphorylation at Ser278 is important for AtRGS1 role in plant immunity[71]. In addition to phosphorylation sites implicated in immune responses, previous studies showed that UDPG-induced AtRGS1 internalization depends on phosphorylation of Ser427, Ser428, Ser431, and Ser435. Phosphorylation at these residues also regulates the interaction of AtRGS1 with the heterotrimeric G protein subunits GPA1, AGB1, and AGG1[12]. These studies, together with our findings here, demonstrate that AtRGS1 undergoes multisite phosphorylation, with distinct phosphorylation events contributing to diverse biological processes, including receptor internalization, protein–protein interactions, and immune signaling.

To fully understand how these phosphorylation sites respond to flg22 and UDPG treatment, we then used DIA phosphoproteomics to analyze our samples. The initial TMT-DDA phosphoproteomic analysis identified only two AtRGS1 phosphosites, Ser278 and Ser430, limiting our ability to assess the broader phosphorylation response of AtRGS1 to flg22 and UDPG. Compared with DDA, DIA provides broader phosphoproteome coverage, higher reproducibility, and more accurate quantification[72]. We therefore performed an independent DIA-based phosphoproteomic analysis to improve phosphosite coverage and further characterize ligand-responsive AtRGS1 phosphorylation. We found 6 phosphorylation sites from AtRGS1, phosphorylation of Ser278 decreased under both flg22 and UDPG treatments. Phosphorylation at Tyr427, Ser428, Ser430, and Ser431 increased in response to both treatments. Notably, flg22 triggered a stronger and more rapid increase in Ser430 phosphorylation compared to UDPG, whereas UDPG induced a greater and faster phosphorylation at Tyr427 and Ser428 than flg22 (**Supplemental Information Figure S8**). Phosphorylation at Ser435 was not detected under flg22 (5 min) or UDPG (5 and 10 min) treatments (**Supplemental Information Figure S8**), raising the possibility that Ser435 undergoes dephosphorylation during both treatments. Collectively, these findings suggest that the phosphorylation pattern across these residues integrates immune and nutrient cues in a treatment- and time-dependent manner.

Signaling bias: Separate cellular trafficking trajectories

AtRGS1 rapidly traffics to the nucleus upon flg22 treatment, where transcriptional reprogramming is shown to occur. In contrast, the trafficking route and ultimate destination of AtRGS1 following UDPG treatment could not be resolved from the FAPβ-AtRGS1 microscopy data, although the observed reduction in plasma membrane-localized AtRGS1 suggests that the protein may undergo degradation. Consistent with these observations, proximity labeling data showed that while flg22 treatment preferentially enriched GO terms associated with transcriptional regulation (Fig. 4G), UDPG treatment was strongly associated with protein degradation-related terms (Fig. 4H). Together, these results suggest that AtRGS1 may participate in flg22-induced transcriptional reprogramming, while UDPG treatment may instead promote AtRGS1 turnover or degradation.

DISCUSSION

We first address here the notion published by previous studies that proximity labeling using APEX2 may not be possible in plant cells due to the poor membrane permeability of biotin phenol, the high abundance of endogenous reactive oxygen species, and the toxicity of H_2O_2[73–75]. In addition, the presence of 73 peroxidase genes in the Arabidopsis genome[76] further raises concerns about the applicability of APEX2 in plant proximity labeling experiments. Indeed, success requires careful optimization of the labeling conditions (times, H_2O_2 and biotin-label concentrations, (**Supplemental Information Figure S4A-D**) along with use of the statistically-determined minimum number of replicates and appropriate controls. Background biotinylation is clearly present (**Supplemental Information Figure S4A-D**). To determine an appropriate significance threshold for the proximity-labeling dataset, we compared the p-value distributions of treatment-responsive proteins identified in APEX2 and WT samples. Because WT samples represent background responses not associated with AtRGS1-directed proximity labeling, we expected a meaningful cutoff to retain proteins preferentially enriched in the APEX2 dataset while excluding those similarly detected in WT controls. We therefore used a two-sample Kolmogorov–Smirnov (KS) test to assess whether the APEX2 and WT p-value distributions differed and used this comparison, together with the relative number of proteins passing candidate thresholds in APEX2 vs. WT, to select an empirical p-value cutoff for downstream analyses. (**Supplemental Information Figure S4E**, Fig. 4C).

The combination of our flg22- and UDPG-induced AtRGS1-proxitome, the AtRGS1 interactome, the AtRGS1 phosphoproteome, and the AtRGS1 transcriptome is the first of its kind in multi-omics approaches to dissect signaling bias in a complex signaling network. The signaling network here represents a central signaling core that integrates at least two vastly different signal types, one a bacterial peptide and the other a sugar metabolite, to propagate disparate signal transduction. flg22 induces a massive change in the phosphoproteome whereas UDPG does not. UDPG induces a massive change in the core neighborhood components whereas flg22 does not. Both are dependent on AtRGS1, a novel receptor-like constituent of the G protein complex.

Following prolonged flg22 treatment, we observed nuclear localization of AtRGS1. This suggests that plasma membrane (PM)-localized AtRGS1 is internalized after flg22 exposure, although the process

appears to take longer than the response to UDPG. Because UDPG binds AtRGS1, we propose that flg22 does not directly affect AtRGS1. Instead, flg22 may act through an intermediate molecule—such as phosphatidic acid (PA), which has been shown to interact with AtRGS1[77]. Notably, flg22 is known to increase endogenous PA levels[78], which may in turn directly regulate AtRGS1 dynamics.

The responses induced by flg22 and UDPG are fast, too fast for most proximity labeling tags. This limited our approach to use APEX2 as our tag on AtRGS1. While APEX2 has the most rapid labeling properties among proximity labeling tags, the abundance of plant peroxidases creates challenges using this labeling agent. Therefore, to identify high-confidence AtRGS1 interactors, we first compared the abundance of biotinylated proteins between the APEX2-expressing line and the WT under control conditions. Proteins with p-values below 0.16 were considered potential interactors based on the proximity labeling data. We then cross-referenced these candidates with proteins identified in the AtRGS1 pulldown experiments. Proteins detected in both datasets were designated as high-confidence AtRGS1 interactors (**Data Set S5 AtRGS1 Potential Partners**).

We observed that UDPG and flg22 rapidly trigger distinct AtRGS1-mediated responses. Brief exposure to UDPG led to depletion of AtRGS1 from the PM. In contrast, brief flg22 treatment induced AtRGS1-dependent phosphorylation events. Previous studies at the protein level showed a strong correlation between AtRGS1 and brassinosteroid (BR) signaling components, including BAK1[18,19]. A transcriptomic study further supported this link, revealing that loss of BAK1 leads to reduced expression of AtRGS1[79], reinforcing the functional association between BAK1 and AtRGS1. In our phosphoproteomics data, we found that phosphorylation of threonine 455 (T455) on BAK1 increased after 10 minutes of flg22 treatment in *rgs1-2* mutants, but not in WT plants. This suggests that AtRGS1 may act as a repressor of BAK1 T455 phosphorylation under flg22 stimulation. We speculate that upon flg22 treatment, AtRGS1 recruits a phosphatase to dephosphorylate BAK1 at T455. However, we do not rule out an alternative mechanism in which AtRGS1 prevents phosphorylation by blocking access of protein kinases to T455.

To reconstruct one of several plausible AtRGS1-mediated signaling pathway response to flg22, we used network analyses of transcription related proteins identified from AtRGS1-dependent phosphosites from the phosphoproteomic data and the AtRGS1-dependent genes from the transcriptomic data. CDC5 and its potential regulated genes were found in this network (**Supplemental Information Figure S9A**). Among the genes potentially regulated by CDC5, there are 7 genes that have been reported to be downregulated by BL treatment[38]. GPA1 mediates BR signaling[80] and controls BR-related proteins in response to sugar[81] and flg22[18]. These 7 genes are under the regulation of a BR and G-protein complex. This prompted building a circuit model with AtRGS1 as the core (**Supplemental Information Figure S9B**). We speculate that the UDPG signal induces AtRGS1 endocytosis toward autophagosomes containing ATG8E. We speculate the following scenario: 1) flg22 induces disassociation of PRL1 from the circuit, 2) flg22 promotes CDC5 phosphorylation which is modulated by AtRGS1, and 3) phosphorylation of CDC5 upregulates the expression of BR- and flg22-responsive genes.

Aside from addressing the mechanism of AtRGS1-dependent signaling bias by flg22 and UDPG, our findings revealed an AtRGS1-mediated feedback mechanism in BR signaling, responsive to flg22-induced stress. The genes in our model were upregulated under flg22 treatment but downregulated under BL treatment, and the loss of AtRGS1 attenuated both the amplitude and timing of these changes, suggesting a AtRGS1 role in the tradeoff between plant immunity and growth.

Declarations

Conflict of Interest

The authors declare no conflict of interest.

Author Contributions

E.S. and Z.L. performed experiments and E.S., Z.L. A.M.J. and J.W.W. interpreted the results. A.M.J and J.W.W. managed different aspects of the project. Z.L., J.W.W and A.M.J. wrote the text and designed the figures. A.M.J. managed the entire project.

ACKNOWLEDGMENTS

We thank Leslie Hicks (UNC) for help in the pilot project. We thank Khem Ghusinga (UNC) for performing the experiments described in Supplemental Information S2. Funding of this project was from a grant from The Division of Chemical Sciences, Geosciences, and Biosciences, Office of Basic Energy Sciences of the US Department of Energy through the grant DE-FG02-05er15671 to A.M.J. Funding was also provided by NIGMS (R01GM065989) and NSF (MCB-0718202) awarded to A.M.J., and by the Iowa State University Plant Science Institute, DOE (DE-SC0023158), NIH (R01GM120316), and USDA NIFA Hatch (IOW04108) funds to J.W.W..

DATA AVAILABILITY

The mass spectrometry proteomics data are available via the ProteomeXchange Consortium at http://proteomecentral.proteomexchange.org via the PRIDE partner repository with the dataset identifier for DDA phosphoproteome data PXD085086; DDA PL data PXD085116; DDA IPMS data PXD085118; DIA phosphoproteome data PXD085130. The RNA-seq data are available via the Sequence Read Archive from NCBI with Bioproject ID PRJNA1538900.

References

1. Mudgil Y et al (2016) Photosynthate regulation of the root system architecture mediated by the heterotrimeric G protein complex in Arabidopsis. Front Plant Sci 7:1255
2. Urano D, Jackson D, Jones AM (2015) AG protein alpha null mutation confers prolificacy potential in maize. J Exp Bot 66:4511–4515
3. Mudgil Y et al (2009) Arabidopsis N-MYC DOWNREGULATED-LIKE1, a positive regulator of auxin transport in a G protein–mediated pathway. Plant Cell 21:3591–3609
4. Chen J-G, Gao Y, Jones AM (2006) Differential roles of Arabidopsis heterotrimeric G-protein subunits in modulating cell division in roots. Plant Physiol 141:887–897
5. Ullah H et al (2003) The β-subunit of the Arabidopsis G protein negatively regulates auxin-induced cell division and affects multiple developmental processes. Plant Cell 15:393–409
6. Chen J-G et al (2003) A seven-transmembrane RGS protein that modulates plant cell proliferation. Science 301:1728–1731
7. Urano D et al (2012) Endocytosis of the seven-transmembrane RGS1 protein activates G-protein-coupled signalling in Arabidopsis. Nat Cell Biol 14:1079–1088
8. Grigston JC et al (2008) D-Glucose sensing by a plasma membrane regulator of G signaling protein, AtRGS1. FEBS Lett 582:3577–3584
9. Chen J-G, Jones AM (2004) AtRGS1 function in Arabidopsis thaliana. Methods Enzymol 389:338–350
10. Johnston CA et al (2007) GTPase acceleration as the rate-limiting step in Arabidopsis G protein-coupled sugar signaling. *Proceedings of the National Academy of Sciences* 104, 17317–17322
11. Fu Y et al (2014) Reciprocal encoding of signal intensity and duration in a glucose-sensing circuit. Cell 156:1084–1095
12. Jia H et al (2025) UDP-glucose Activation of a G-protein/Sucrose Synthase Signaling Supercomplex. *bioRxiv*, 2009. 2010.672744 (2025)
13. Watkins JM et al (2021) Differential regulation of G protein signaling in Arabidopsis through two distinct pathways that internalize AtRGS1. Sci Signal 14:eabe4090
14. Smith JS, Lefkowitz RJ, Rajagopal S (2018) Biased signalling: from simple switches to allosteric microprocessors. Nat Rev Drug Discovery 17:243–260
15. Sun Y et al (2013) Structural basis for flg22-induced activation of the Arabidopsis FLS2-BAK1 immune complex. Science 342:624–628
16. Tunc-Ozdemir M, Urano D, Jaiswal DK, Clouse SD, Jones AM (2016) Direct modulation of heterotrimeric G protein-coupled signaling by a receptor kinase complex. J Biol Chem 291:13918–13925
17. Watkins JM et al (2024) Phosphorylation Dynamics in a flg22-Induced, G Protein–Dependent Network Reveals the AtRGS1 Phosphatase. Mol Cell Proteom 23
18. Liang X et al (2018) Ligand-triggered de-repression of Arabidopsis heterotrimeric G proteins coupled to immune receptor kinases. Cell Res 28:529–543

19. Tunc-Ozdemir M, Jones AM (2017) Ligand-induced dynamics of heterotrimeric G protein-coupled receptor-like kinase complexes. PLoS ONE 12:e0171854
20. Tunc-Ozdemir M et al (2017) Predicted functional implications of phosphorylation of regulator of G protein signaling protein in plants. Front Plant Sci 8:1456
21. Xing J, Ji D, Duan Z, Chen T, Luo X (2022) Spatiotemporal dynamics of FERONIA reveal alternative endocytic pathways in response to flg22 elicitor stimuli. New Phytol 235:518–532
22. Rich-Griffin C et al (2020) Regulation of cell type-specific immunity networks in Arabidopsis roots. Plant Cell 32:2742–2762
23. Bethke G et al (2009) Flg22 regulates the release of an ethylene response factor substrate from MAP kinase 6 in Arabidopsis thaliana via ethylene signaling. *Proceedings of the National Academy of Sciences* 106, 8067–8072
24. Blanco-Herrera F et al (2015) The UDP-glucose: glycoprotein glucosyltransferase (UGGT), a key enzyme in ER quality control, plays a significant role in plant growth as well as biotic and abiotic stress in Arabidopsis thaliana. BMC Plant Biol 15:1–12
25. Wubben MJ, Rodermel SR, Baum TJ (2004) Mutation of a UDP-glucose-4-epimerase alters nematode susceptibility and ethylene responses in Arabidopsis roots. Plant J 40:712–724
26. Meng M et al (2009) UDP-glucose pyrophosphorylase is not rate limiting, but is essential in Arabidopsis. Plant Cell Physiol 50:998–1011
27. Handford M et al (2012) Arabidopsis thaliana AtUTr7 encodes a golgi-localized UDP–Glucose/UDP–galactose transporter that affects lateral root emergence. Mol Plant 5:1263–1280
28. Zhang Y et al (2019) TurboID-based proximity labeling reveals that UBR7 is a regulator of N NLR immune receptor-mediated immunity. Nat Commun 10:3252
29. Song G, Montes C, Walley JW (2020) Quantitative profiling of protein abundance and phosphorylation state in plant tissues using tandem mass tags. Plant proteomics: methods protocols, 147–156
30. Bolger AM, Lohse M, Usadel B (2014) Trimmomatic: a flexible trimmer for Illumina sequence data. Bioinformatics 30:2114–2120. 10.1093/bioinformatics/btu170
31. Liao Y, Smyth GK, Shi W (2013) featureCounts: an efficient general purpose program for assigning sequence reads to genomic features. Bioinformatics 30:923–930. 10.1093/bioinformatics/btt656
32. Love MI, Huber W, Anders S (2014) Moderated estimation of fold change and dispersion for RNA-seq data with DESeq2. Genome Biol 15:1–21
33. Xu S et al (2024) Using clusterProfiler to characterize multiomics data. Nat Protoc 19:3292–3320
34. Cox J, Mann M (2008) MaxQuant enables high peptide identification rates, individualized ppb-range mass accuracies and proteome-wide protein quantification. Nat Biotechnol 26:1367–1372
35. Zhu Y et al (2020) DEqMS: a method for accurate variance estimation in differential protein expression analysis. Mol Cell Proteom 19:1047–1057

36. Tyanova S et al (2016) The Perseus computational platform for comprehensive analysis of (prote) omics data. Nat Methods 13:731–740
37. Plubell DL et al (2017) Extended multiplexing of tandem mass tags (TMT) labeling reveals age and high fat diet specific proteome changes in mouse epididymal adipose tissue. Mol Cell Proteom 16:873–890
38. Clark NM et al (2021) Integrated omics networks reveal the temporal signaling events of brassinosteroid response in Arabidopsis. Nat Commun 12:5858
39. Clark N (2023) *nmclark2/SCION: Version 4.1*Zenodo
40. Bauer Z, Gómez-Gómez L, Boller T, Felix G (2001) Sensitivity of different ecotypes and mutants ofArabidopsis thaliana toward the bacterial elicitor flagellin correlates with the presence of receptor-binding sites. J Biol Chem 276:45669–45676
41. Boeck JM, Spencer JV (2017) Effect of human cytomegalovirus (HCMV) US27 on CXCR4 receptor internalization measured by fluorogen-activating protein (FAP) biosensors. PLoS ONE 12:e0172042
42. Gallo E (2019) Fluorogen-activating proteins: next-generation fluorescence probes for biological research. Bioconjug Chem 31:16–27
43. Boivin B, Vaniotis G, Allen BG, Hebert TE (2008) G protein-coupled receptors in and on the cell nucleus: a new signaling paradigm? J Recept Signal Transduction 28:15–28
44. Allen BG, Merlen C, Branco AF, Pétrin D, Hébert TE (2024) Understanding the impact of nuclear-localized GPCRs on cellular signalling. Cell Signal 123:111358
45. Bhosle VK, Rivera JC, Chemtob S (2019) New insights into mechanisms of nuclear translocation of G-protein coupled receptors. Small GTPases 10:254–263
46. Huang J, Fisher RA (2009) Nuclear trafficking of regulator of G protein signaling proteins and their roles in the nucleus. Prog Mol Biol Transl Sci 86:115–156
47. Park HJ et al (2023) S-acylated and nucleus-localized SALT OVERLY SENSITIVE3/CALCINEURIN B-LIKE4 stabilizes GIGANTEA to regulate Arabidopsis flowering time under salt stress. Plant Cell 35:298–317
48. Li Y et al (2022) Plasma membrane-nucleo-cytoplasmic coordination of a receptor-like cytoplasmic kinase promotes EDS1-dependent plant immunity. Nat Plants 8:802–816
49. Kohorn BD, Hoon D, Minkoff BB, Sussman MR, Kohorn SL (2016) Rapid oligo-galacturonide induced changes in protein phosphorylation in Arabidopsis. Mol Cell Proteom 15:1351–1359
50. Rayapuram N et al (2014) Identification of novel PAMP-triggered phosphorylation and dephosphorylation events in Arabidopsis thaliana by quantitative phosphoproteomic analysis. J Proteome Res 13:2137–2151
51. Nühse TS, Bottrill AR, Jones AM, Peck SC (2007) Quantitative phosphoproteomic analysis of plasma membrane proteins reveals regulatory mechanisms of plant innate immune responses. Plant J 51:931–940

52. Benschop JJ et al (2007) Quantitative phosphoproteomics of early elicitor signaling in Arabidopsis. Mol Cell Proteom 6:1198–1214
53. Jia H et al (2025) Phosphorylation-activated G protein signaling stabilizes TCP14 and JAZ3 to repress JA signaling and enhance plant immunity. Mol Plant 18:1171–1192
54. Li D et al (2022) An evaluation of RNA-seq differential analysis methods. PLoS ONE 17:e0264246
55. Jones JC, Temple BR, Jones AM, Dohlman HG (2011) Functional reconstitution of an atypical G protein heterotrimer and regulator of G protein signaling protein (RGS1) from Arabidopsis thaliana. J Biol Chem 286:13143–13150
56. Asai T et al (2002) MAP kinase signalling cascade in Arabidopsis innate immunity. Nature 415:977–983
57. Nühse TS, Peck SC, Hirt H, Boller T (2000) Microbial elicitors induce activation and dual phosphorylation of the Arabidopsis thaliana MAPK 6. J Biol Chem 275:7521–7526
58. van Wijk KJ, Friso G, Walther D, Schulze W (2014) X. Meta-analysis of Arabidopsis thaliana phospho-proteomics data reveals compartmentalization of phosphorylation motifs. Plant Cell 26:2367–2389
59. Guo X, Ding X, Dong J (2022) Dichotomy of the BSL phosphatase signaling spatially regulates MAPK components in stomatal fate determination. Nat Commun 13:2438
60. He Z, Webster S, He SY (2022) Growth–defense trade-offs in plants. Curr Biol 32:R634–R639
61. Xie Z, Klionsky DJ (2007) Autophagosome formation: core machinery and adaptations. Nat Cell Biol 9:1102–1109
62. Nam KH, Li J (2002) BRI1/BAK1, a receptor kinase pair mediating brassinosteroid signaling. Cell 110:203–212
63. Wang S et al (2025) CLE19 suppresses brassinosteroid signaling output via the BSL-BIN2 module to maintain BES1 activity and pollen exine patterning in Arabidopsis. J Integr Plant Biol 67:3216–3230
64. Mora-García S et al (2004) Nuclear protein phosphatases with Kelch-repeat domains modulate the response to brassinosteroids in Arabidopsis. Genes Dev 18:448–460
65. Liu X, Salokas K, Weldatsadik RG, Gawriyski L, Varjosalo M (2020) Combined proximity labeling and affinity purification– mass spectrometry workflow for mapping and visualizing protein interaction networks. Nat Protoc 15:3182–3211
66. Larochelle M, Bergeron D, Arcand B, Bachand F (2019) Proximity-dependent biotinylation mediated by TurboID to identify protein–protein interaction networks in yeast. J Cell Sci 132:jcs232249
67. Lambert J-P, Tucholska M, Go C, Knight JD, Gingras A-C (2015) Proximity biotinylation and affinity purification are complementary approaches for the interactome mapping of chromatin-associated protein complexes. J Proteom 118:81–94
68. do Moreira N (2023) Impact of inherent biases built into proteomic techniques: Proximity labeling and affinity capture compared. J Biol Chem 299:102726
69. Su B, Wang A, Xie D, Shan X (2023) VA-TIRFM-based SM kymograph analysis for dwell time and colocalization of plasma membrane protein in plant cells. Plant Methods 19:70

70. Palma K et al (2007) Regulation of plant innate immunity by three proteins in a complex conserved across the plant and animal kingdoms. Genes Dev 21:1484–1493
71. Oliveira CC et al (2025) A molecular dynamics study of membrane positioning for 7-transmembrane RGS proteins to modulate G-protein-mediated signaling in plants. Comput Struct Biotechnol J 27:1529–1537
72. Bekker-Jensen DB et al (2020) Rapid and site-specific deep phosphoproteome profiling by data-independent acquisition without the need for spectral libraries. Nat Commun 11:787
73. Xu S-L, Shrestha R, Karunadasa SS, Xie P-Q (2023) Proximity labeling in plants. Annu Rev Plant Biol 74:285–312
74. Mair A, Bergmann DC (2022) Advances in enzyme-mediated proximity labeling and its potential for plant research. Plant Physiol 188:756–768
75. Samavarchi-Tehrani P, Samson R, Gingras A-C (2020) Proximity dependent biotinylation: key enzymes and adaptation to proteomics approaches. Mol Cell Proteom 19:757–773
76. Tognolli M, Penel C, Greppin H, Simon P (2002) Analysis and expression of the class III peroxidase large gene family in Arabidopsis thaliana. Gene 288:129–138
77. Roy Choudhury S, Pandey S (2017) Phosphatidic acid binding inhibits RGS 1 activity to affect specific signaling pathways in Arabidopsis. Plant J 90:466–477
78. van der Luit AH et al (2000) Elicitation of suspension-cultured tomato cells triggers the formation of phosphatidic acid and diacylglycerol pyrophosphate. Plant Physiol 123:1507–1516
79. Wu Y et al (2020) Loss of the common immune coreceptor BAK1 leads to NLR-dependent cell death. *Proceedings of the National Academy of Sciences* 117, 27044–27053
80. Ullah H, Chen J-G, Wang S, Jones AM (2002) Role of a heterotrimeric G protein in regulation of Arabidopsis seed germination. Plant Physiol 129:897–907
81. Peng Y et al (2018) BRI1 and BAK1 interact with G proteins and regulate sugar-responsive growth and development in Arabidopsis. Nat Commun 9:1522

Figures

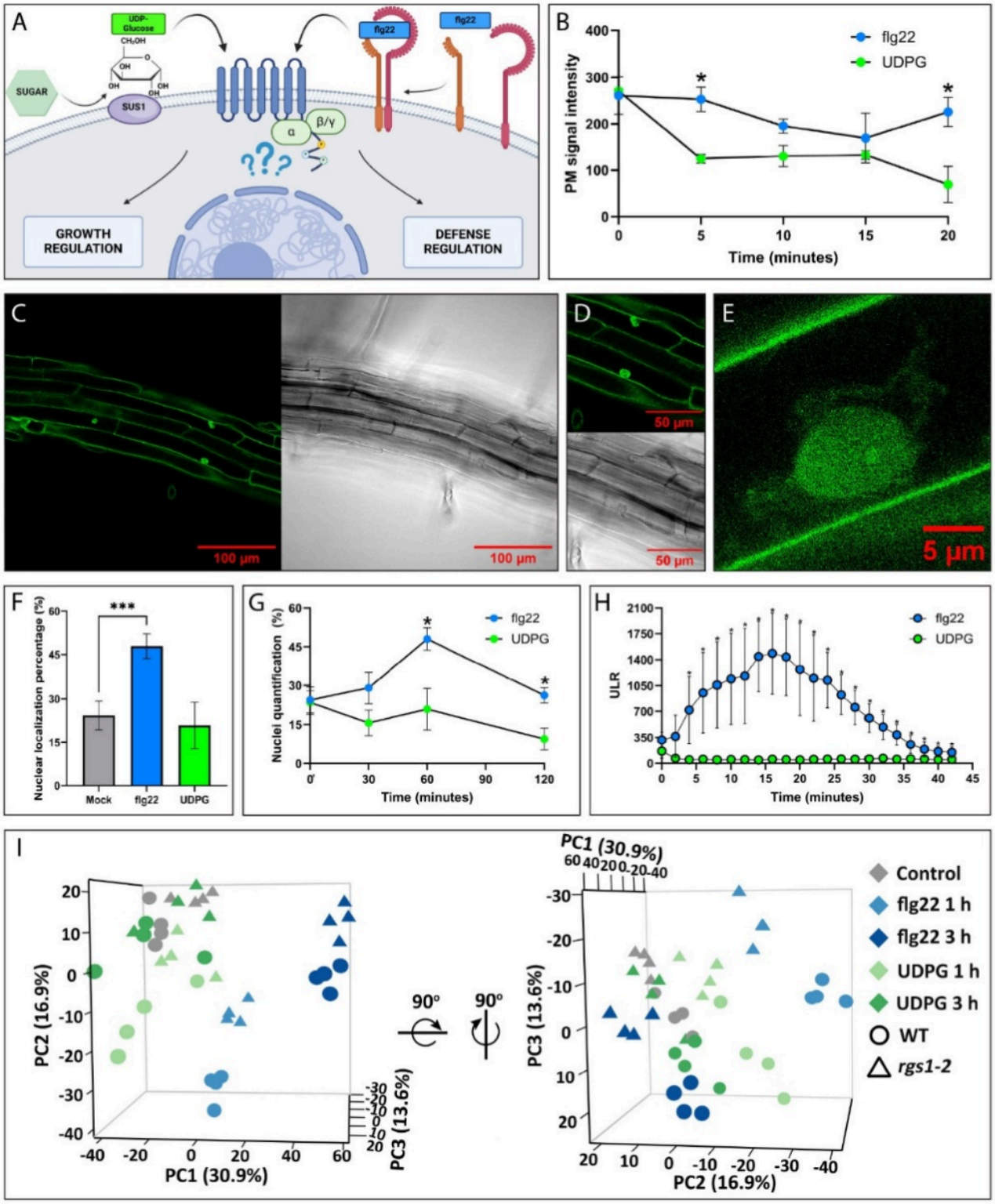


Figure 1

Biased flg22 and UDP-Glucose signaling in Arabidopsis roots.

(**A**) Working Hypothesis. Illustration of the biased signaling output through AtRGS1 in response to flg22 and UDPG, highlighting the main individual components involved in this mechanism and the presumed sequence of events known at this time.

(**B**) Both signals cause rapid internalization of FAPβ-AtRGS1. PM signaling intensity over time under

flg22 (blue) and UDPG (green) induction. Error bars indicate the StDev.
(**C**) Representative processed confocal images of FAPβ-AtRGS1 cellular localization under flg22 treatment. Left is a fluorescence and right is a DIC microscopy image. Scale bar = 100 μm
(**D**) High-magnification confocal image of FAPβ-AtRGS1 cellular localization under flg22 treatment. Top is a fluorescence and bottom is a DIC microscopy image. Scale bar = 50 μm
(**E**) Representative nucleus containing FAPβ-AtRGS1. Scale bar = 5 μm.

Average nuclear quantification across treatments after 1 hour of exposure.
(**F**) Nuclear FAPβ-AtRGS1 quantification under mock, flg22, and UDPG 1-h treatments. Error bars represent the StDev. Asterix between the indicated treatments indicates statistical difference ($p < 0.001$).
(**G**) Dose response of flg22 and UDPG on AtRGS1 nuclear localization. Shown are the percent of nuclei that contain AtRGS1-YFP at the indicated time after treatment with flg22 (blue) and with UDPG (green). Error bar = StDev. Asterisk indicates statistical difference from time zero with confidence of $p < 0.001$.

(H) ROS burst elicited by flg22 (blue) and UDPG (green). Details of this experiment are described in Methods.
(**I**) PCA of transcriptome showing WT (circles) and *rgs1-2* mutant (triangles) under different conditions indicated by the colors in the diamond shapes of the inset: specifically, gray for control, light blue for 60 min flg22 treatment, dark blue for 180 min flg22 treatment, light green 60 min UDPG, and dark green for 180 min UDPG.

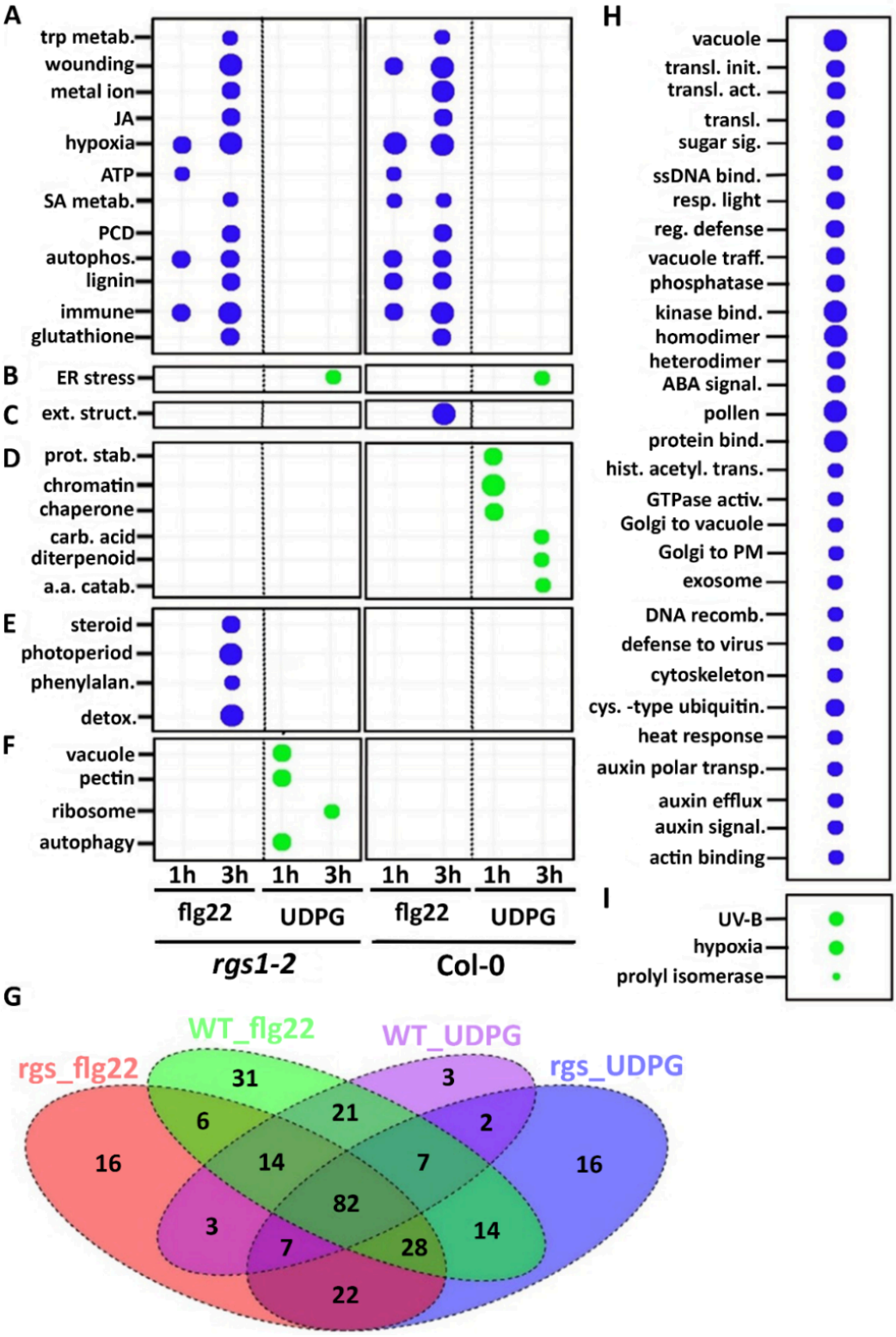


Figure 2

flg22 and UDPG launch different biological processes.

(**A**) GO transcriptome functions initiated by flg22 only

(**B**) GO transcriptome functions initiated by UDPG only

(**C**) AtRGS1-dependent transcriptome GO functions initiated by flg22 only

(**D**) AtRGS1-dependent transcriptome GO functions initiated by UDPG only

(**E**) GO transcriptome functions initiated by flg22 only that are negatively regulated by AtRGS1

(**F**) GO transcriptome functions initiated by UDPG only that are negatively regulated by AtRGS1

(**A-F**) Genes from differential analysis with adjusted p-value less than 0.05 were chosen for ORA and GO biological process analysis; Y axis shows GO biological process catalogs; x axis shows different treatment, flg22_1h means 100 nM flg22 treated for 1 hour, flg22_3h means 100 nM flg22 treated for 3 hour, UDPG_1h means 123 μM UDPG treated for 1 hour, UDPG_3h means 123 μM UDPG treated for 3 hour; the gene counts belong to different catalogs were log2 transformed as shown in log2Count; statistics analysis was done with fisher's exact test, and Benjamini-Hochberg procedure was used for multiple comparison adjustment. Blue circles represent enrichment by flg22 and green circles represent enrichment by UDPG. The size of the circle qualitatively represents the number of hits where the largest circle is in the range of log2 exp. 6-7 and the smallest circle is log2 exp 3-4. Exact hit numbers as well as the associated P values are provided in **Data set S1 Transcriptome, sheet ORA_GO_BP.**

Terms for GO category: ribosome, ribosome assembly; vacuole, vacuole organization; detox, detoxification; phenylalan., L-phenylalanine metabolic process; pectin, pectin metabolic process; carb. Acid, carboxylic acid catabolism process; prot. Stab., protein stability; ER stress, response to endoplasmic reticulum stress; glutathione, glutathione metabolic process; immune, immune response; lignin, lignin metabolic process; autophos., protein autophosphorylation; PCD, programmed cell death; SA metab., regulation of salicylic acid metabolic process; ATP, response to ATP; hypoxia, response to hypoxia; JA, response to jasmonic acid; metal ion, response to metal ion; ext. struct., external encapsulating structure organization

(**G**) flg22- and UDPG-induced phosphoproteome GO functions, both dependent on and independent of AtRGS1. Venn diagram shows the number of enriched GO terms under flg22 (**_flg22**) and UDPG (**_UDPG**) in the *rgs1*-2 mutant (**rgs_**) and Col-0 (**WT_**) backgrounds.

(**H**) GO functions of flg22-induced changes in protein phosphorylation that only found in WT plants. The size of the circle qualitatively represents the number of hits where the largest circle is in the range of log2 exp. 4 and the smallest circle is log2 exp 3.6. Exact hit numbers as well as the associated q values are provided in **Data set S2 Phosphoproteome, GO_of_WT_flg22_only**.

(**I**) GO functions of UDPG-induced changes in protein phosphorylation that only found in WT plants. The size of the circle qualitatively represents the number of hits where the largest circle is in the range of log2 exp. 6-7 and the smallest circle is log2 exp 3-4. Exact hit numbers as well as the associated q values are provided in **Data set S2 Phosphoproteome, GO_of_WT_UDPG_only**. (**H-I**) Terms for GO category: transl. init., translational initiation; transl. act., translational initiation factor or activity; transl., translation; sugar sig., sugar mediated signaling pathway; ssDNA bind., single-stranded DNA binding;

resp. light, responses to light stimulus; reg. defense, regulation of defense response; vacuole traff., protein targeting to vacuole; phosphatase, protein phosphatase regulator activity; kinase bind., protein kinase binding and kinase binding (two categories); homodimer., protein homodimerization activity; heterodimer., protein heterodimerization activity; ABA signal., positive regulation of abscisic acid-activated signaling pathway; pollen, pollen development; protein bind., identical protein binding; hist. acetyl. Trans., histone acetyltransferase activity; GTPase active, GTPase activator activity; Golgi to vacuole, Golgi to vacuole transport; Golgi to PM, Golgi to plasma membrane transport; exosome, extracellular exosome; DNA recomb., DNA recombination; defense to virus, defense response to virus; cys.-type ubiquitin., cysteine-typeubiquitination; heat response, cellular response to heat; auxin polar transp., auxin polar transport; auxin signal., auxin efflux transmembrane transporter activity; auxin signal., auxin-activated signaling pathway.

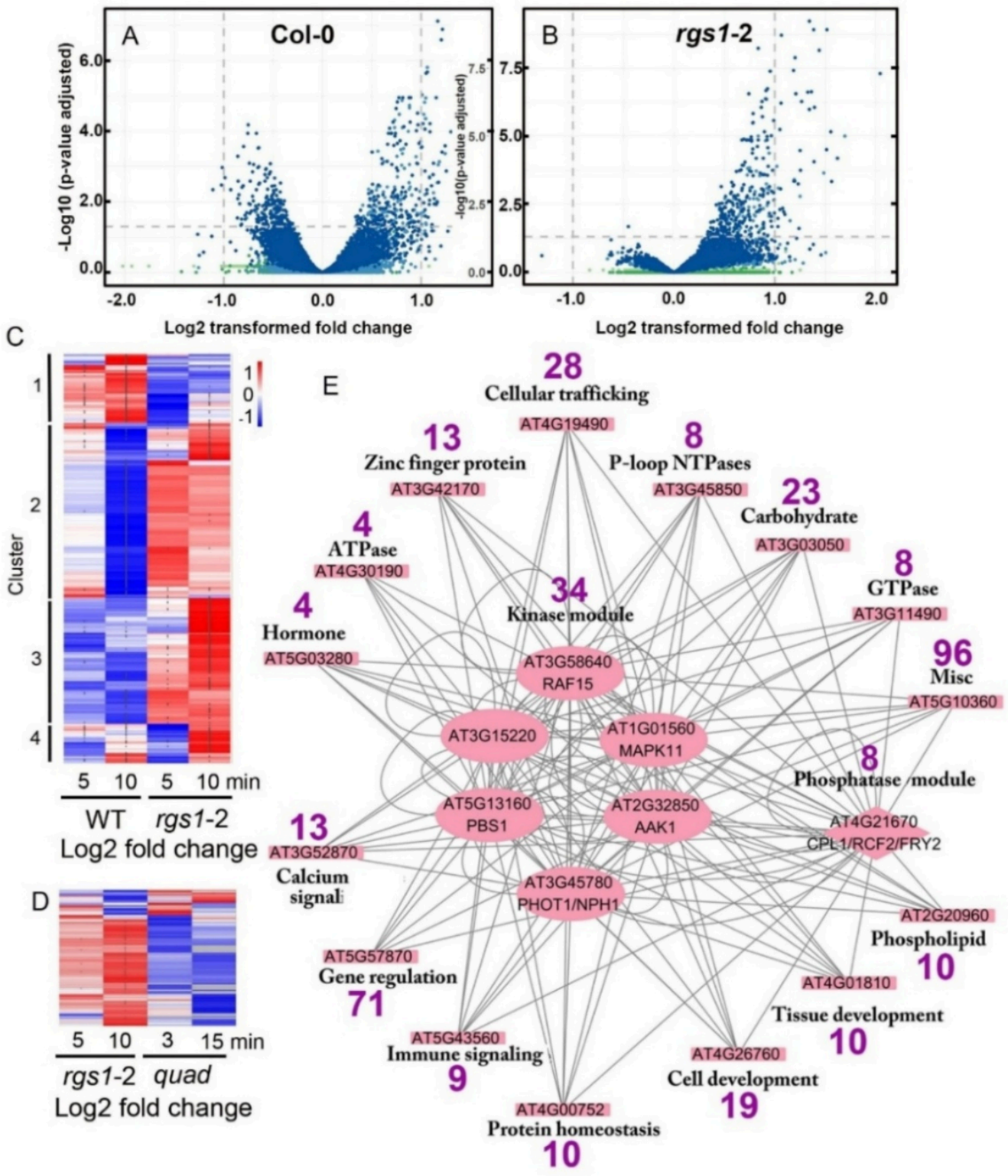


Figure 3

Signaling bias through AtRGS1: flg22, but not UDPG, causes a massive reprogramming of the phosphoproteome.

(**A**) Volcano plot of different treatment groups versus control groups from WT plants phosphoproteome. X axis is the value of log2 transformed fold change; y axis is the value of –log10 transformed adjusted p-

value; horizontal gray dot line shows where adjusted p-value equals to 0.05; vertical gray dot lines show where log2 fold change is -1 (left) and 1 (right); Light blue is 5 minutes 100 nM flg22 treatment versus control group; dark blue is 10 minutes 100 nM flg22 treatment versus control group; light green is 5 minutes 123 μM UDPG versus control group; dark green is 10 minutes 123μM UDPG treatment versus control group; statistics analysis was done with Wald test, and BH procedure was used for multiple comparison adjustment.

(**B**) Volcano plot of different treatment groups versus control groups from *rgs1-2*plants phosphoproteome. X axis is the value of log2 transformed fold change; y axis is the value of –log10 transformed adjusted p-value; horizontal gray dot line shows where adjusted p-value equals to 0.05; vertical gray dot lines show where log2 fold change is -1(left one) and 1(right one); Light blue is log2 fold change between 5 minutes 100 nM flg22 treatment and control group; dark blue is log2 fold change between 10 minutes 100 nM flg22 treatment and control group; light green is log2 fold change between 5 minutes 123 μM UDPG and control group; dark green is log2 fold change between 10 minutes 123 μM UDPG treatment and control group; statistics analysis was done with the Wald test, and the Benjamini-Hochberg procedure was used for multiple comparison adjustment.

(**C**) Heatmap of AtRGS1 and G protein complex dependent phosphosite responses under different flg22 treatment. WT 5min means log2 fold change of phosphosites from WT plants between 5 minutes 100 nM flg22 treatment and control group; WT 10min means log2 fold change of phosphosites from WT plants between 10 minutes 100 nM flg22 treatment and control group; *rgs1*-2 5min means log2 fold change of phosphosites from *rgs1*-2 plants between 5 minutes 100nM flg22 treatment and control group; *rgs1*-2 10 min means log2 fold change of phosphosites from *rgs1*-2 plants between 10 minutes 100 nM flg22 treatment and control group; different clusters were labeled with corresponding numbers 1-4; asterisks indicate BH adjusted p-value less than 0.05; fold change as indicate in scale bar.

(**D**) Heatmap of AtRGS1 and G protein complex dependent phosphosite responses under different flg22 treatment. *rgs1-2* 5min means log2 fold change of phosphosites from *rgs1-2* plants between 5 minutes 100 nM flg22 treatment and control group; *rgs1-2* 10min means log2 fold change of phosphosites from *rgs1-2* plants between 10 minutes 100 nM flg22 treatment and control group; quad 3min means log2 fold change of phosphosites from G protein complex null mutant roots between 3 minutes 100 nM flg22 treatment and control group; quad 10min means log2 fold change of phosphosites from G protein complex mutants between 10 minutes 100 nM flg22 treatment and control group; asterisks indicate BH adjusted p-value less than 0.05; fold change as indicate in scale bar (**Data set S2 Phosphoproteome, Phosphosites_shared_by_2_data)**.

(**E**) AtRGS1-dependent kinase/phosphatase network. Eclipse shows protein kinase, diamond shows protein phosphatase, square shows correlated protein of kinase or phosphatase. All proteins within the network were grouped into different modules as shown in the figure according to their functions. Proteins with high edge count or neighborhood connectivity within each module were highlighted in purple. Numbers in purple show the protein counts within each module, black numbers in parentheses

are the average edge counts for each module. The AtRGS1-dependent kinase/phosphatase network with all protein IDs can be found in **Supplemental Information Figure S7**.

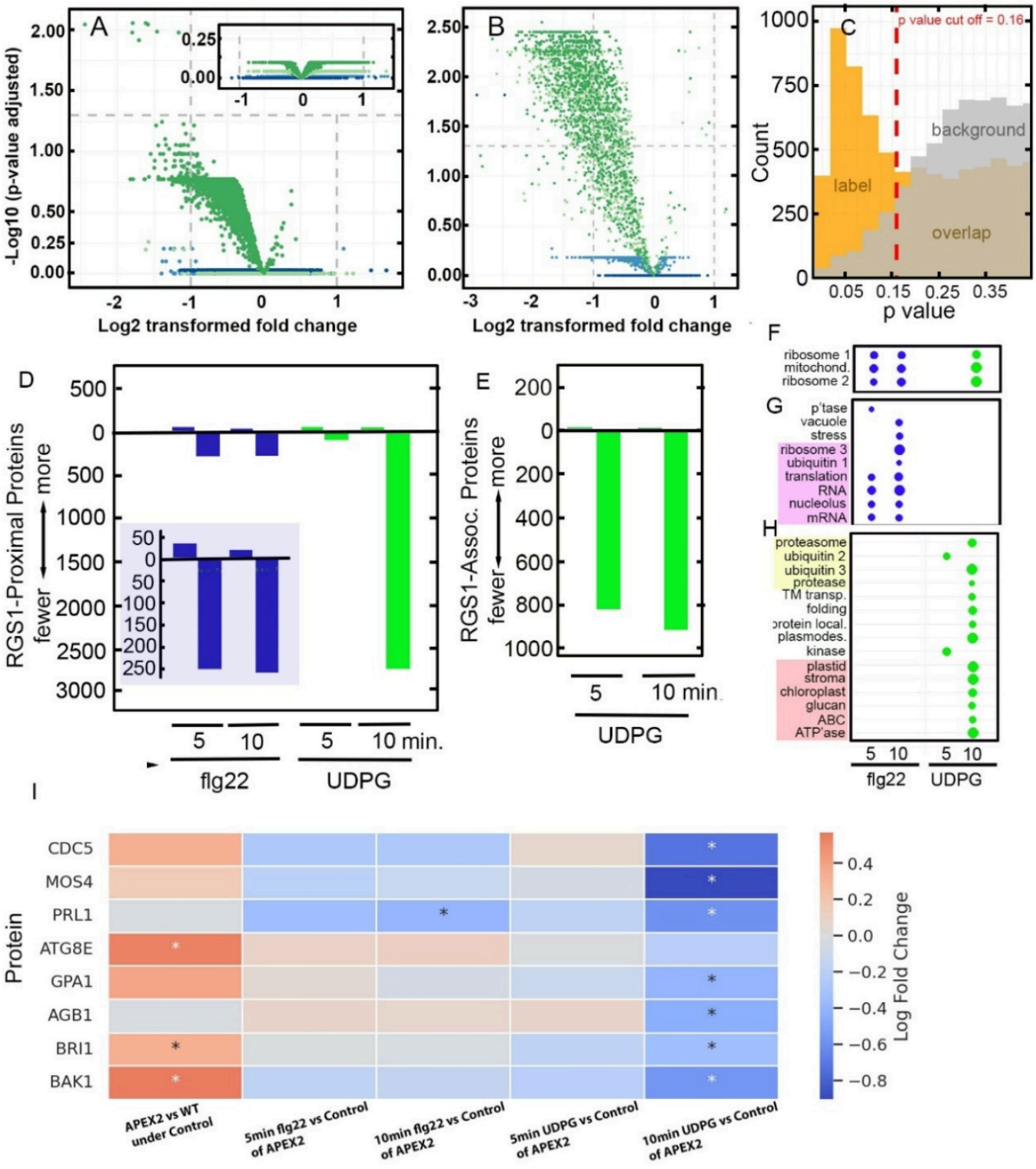


Figure 4

UDPG, but much less so for flg22, induces a massive change in the AtRGS1 neighborhood.

(**A**) Volcano plot of different treatment groups versus control groups from AtRGS1-APEX2 expressing plants and WT plants (inserted plot) in PL experiments. X axis is the value of log2 transformed fold change; y axis is the value of –log10 transformed adjusted p-value; horizontal gray dot line shows where adjusted p-value equals to 0.05; vertical gray dot lines show where log2 fold change is -1(left one) and 1(right one); Light blue is 5 min 100 nM flg22 treatment versus control group; dark blue is 10 min 100 nM flg22 treatment versus control group; light green is 5 minutes 123 μM UDPG versus control group; dark green is 10 min 123 μM UDPG treatment versus control group; statistics analysis was done with Wald test, and Benjamini-Hochberg procedure was used for multiple comparison adjustment.

(**B**) Volcano plot of different treatment groups versus control groups from AtRGS1YFP pulldown experiments. X axis is the value of log2 transformed fold change; y axis is the value of –log10 transformed adjusted p-value; horizontal gray dot line shows where adjusted p-value equals to 0.05; vertical gray dot lines show where log2 fold change is -1(left) and 1(right); Light blue is 5 min 100 nM flg22 treatment versus control group; dark blue is 10 min 100 nM flg22 treatment versus control group; light green is 5 min 123 μM UDPG versus control group; dark green is 10 min 123 μM UDPG treatment versus control group; statistics analysis was done with Wald test, and Benjamini-Hochberg procedure was used for multiple comparison adjustment.

(**C**) Overlay of p-values from WT and AtRGS1-APEX2 expressing lines. Orange line is p-values from AtRGS1-APEX2 expressing lines, gray line is p-values WT lines. X-axis is p-values, y-axis is count number. Red broken line indicates where the cutoff p-value.

(**D**) Differentially expressed protein numbers found in the proximity labeling experiment. Blue are protein numbers found in flg22 treatment, green is protein numbers found in UDPG treatment, different treatment time were shown as the x axis; the highlighted (light blue) insertion panel is the protein numbers found in flg22 treatment plotted separately in order to better illustrate the difference in proximity dynamics between flg22 and UDPG.

(**E**) Differentially expressed protein numbers found in AtRGS1-YFP pulldown experiment. Green is protein numbers found in UDPG treatment, different treatment time were shown as the x axis.

(**F-H**) GO analysis of AtRGS1 proxitome proteins identified from PL experiments. Ribosome 1, structural constituent of ribosome; mitochond., mitochondrion; ribosome 2, cytosolic ribosome; translation, translation; p’tase, protein dephosphorylation; RNA, RNA binding; mRNA, mRNA binding; stress, cellular response to oxidative stress; ubiquitine 1, ubiquitin binding;proteasome, proteasome complex; ubiquitin 2, ubiquitin protein ligase activity; ubiquitin 3, ubiquitin-dependent protein catabolic process; protease, serine-type carboxypeptidase; TM transp., transmembrane transport; protein local., protein localization; folding, protein folding; kinase, kinase activity; plastid, plastid; stroma, chloroplast stroma; chloroplast, envelope; glucan, glucan endo-1,3-beta-D-glucosidase activity; ABC, ATPase-coupled transmembrane transporter activity; ATP’ase, ATP hydrolysis activity. The size of the circle represents the relative log2 count where the smallest circle is in the range of 4-5, and the largest is 8-9. The exact counts are provided **Data Set S3 Proxitome, sheet GO_BP**.

(**I**) Potential AtRGS1-interacted proteins with known functions in G protein signaling, brassinosteroid (BR) signaling, autophagy, and immune responses. The y-axis lists protein names, and the x-axis indicates the treatment conditions used to calculate log2-transformed fold changes. Asterisks indicate $P < 0.16$.

Supplementary Files

This is a list of supplementary files associated with this preprint. Click to download.

- DataSetS3RGS1Proxitome.xlsx
- DataSetS5RGS1PotentialPartners.xlsx
- DataSetS4RGS1interactome.xlsx
- DataSetS2Phosphoproteome.xlsx
- DataSetS1Transcriptome.xlsx
- SupplementalInformationRGS1BIASEDSIGNALINGsubmitted.pdf
- supplementaryfileofuncroppedblots.docx